Quaternary Science Reviews 305 (2023) 107996

Contents lists available at ScienceDirect

Quaternary Science Reviews

journal homepage: www.elsevier.com/locate/quascirev

Robbins Island: The index site for regional Last Interglacial sea level, wave climate and the subtropical ridge around Bass Strait, Australia

Ian D. Goodwin [a, b, c, *], Thomas R. Mortlock [a, b], Marta Ribo [a, d], Jerry X. Mitrovica [e], Mick O' Leary [f], Rory Williams [a]

[a] School of Natural Sciences, Macquarie University, North Ryde, NSW, 2109, Australia
[b] Climate Change Research Centre, University of NSW, Kensington, NSW, Australia
[c] ClimaLab, Newport, NSW, 2106, Australia
[d] Department of Environmental Science, School of Science, Auckland University of Technology, Auckland, New Zealand
[e] Department of Earth Science, Harvard University, Cambridge, MA, USA
[f] Department of Earth Science, University of Western Australia, Perth, Australia

ARTICLE INFO

Article history:
Received 1 September 2022
Received in revised form
30 January 2023
Accepted 5 February 2023
Available online xxx

Handling Editor: I Hendy

Keywords:
Interglacial(s)
Sea level changes
Southern ocean
Geomorphology
Coastal

ABSTRACT

A unique index-record of Last Interglacial (Marine Isotope Stage 5e MIS5e) relative sea level (RSL) and wave climate history in South-east Australia is presented from Robbins Island, in western Bass Strait. This is applied to interpret the wider MIS5e coastal evidence around Bass Strait. At Robbins Island, the combination of low wave and wind energy, a tide-modified regime and a sand supply resulted in the shoreline progradation throughout MIS5e. This preserved a time-series of paleo-sea level across a 7 km wide strandplain (Remarkable Banks). After a highstand, MIS5e RSL attained a stillstand of $+5.75 \pm 0.5$ m above modern mean sea level during 126 to ~119 ka BP. The MIS5e RSL interpretation is underpinned by modern analogues and hydrodynamic modelling of waves, tides and currents. A high resolution LiDAR Digital Elevation Model (DEM) supported by morpho-sedimentary studies, ground-penetration radar (GPR) surveys and a geochronology based upon Optically Stimulated Luminescence (OSL) methods were used to define the proxy RSL record. The observed RSL history was compared to modelled RSL history that accounted for the theoretical fall in RSL (regression) throughout MIS5e, due to the Glacio-Isostatic Adjustment (GIA) forcing.

Three stages of RSL change occurred during MIS 5e: (i) RSL fall during phase 1 from ~129 to 126 ka BP, and during phase 3 between ~118 and 114 ka BP.; and, (ii) a multi-millennial stillstand during the intervening phase 2 from 126 to ~119 ka BP. The stillstand departure from GIA theory, points unambiguously to persistent polar meltwater contributions to sea level of ~2 m from 126 to 119 ka BP, where the component of RSL fall due to GIA was balanced by the RSL rise from meltwater. The potential contributions of paleo wave climate (direction) and boundary current histories were reconstructed from across all Bass Strait sites to determine an RSL budget. In addition, the paleo wave climate history allowed the triangulation of directional ocean wave synoptic sources and identified a 5° poleward shift in the Subtropical Ridge during MIS5e.

1. Introduction

The amount, timing and sources of polar meltwater contributions to Last Interglacial (Marine Isotope Stage 5e MIS5e, 130 to 115 ka BP) sea-levels are poorly constrained (Lambeck et al., 2012; Barlow et al., 2018; Rohling et al., 2019). Best estimates place the total (eustatic and steric) sea-level rise (SLR) during MIS5e to be 6–9 m of sea-level equivalent above modern sea-level (Kopp et al., 2009, 2013). The range and uncertainty in these estimates is produced by: (1) the disparate sources of paleo-sea level observations in near, mid and far-field zones of contrasting response to the Glacio-Isostatic Adjustment (GIA); (2) the post-observation correction according to a range of geophysical parameters such as upper and lower mantle viscosity, lithospheric thickness; and, (3) a poorly-constrained post glacial ice model of meltwater mass and

* Corresponding author. Climate Change Research Centre, University of New South Wales, Kensington, NSW Australia
E-mail address: i.goodwin@unsw.edu.au (I.D. Goodwin).

https://doi.org/10.1016/j.quascirev.2023.107996

rates of supply to the ocean during the MIS6 to MIS5e transition (Lambeck et al., 2012; Rovere et al., 2016). In addition, debate is ongoing as to whether significant input of Polar meltwater to the global ocean ceased in the early MIS5e or continued monotonically or abruptly during late MIS5e (Dutton and Lambeck, 2012; O' Leary et al., 2013; Dutton et al., 2015; Barlow et al., 2018, Dutton et al., 2022). The majority of MIS5e paleo sea-level observations are derived from point in time age-elevation measurements from indurated geological contexts; typically, tidal notches and coral reef structures, and chronological uncertainties makes it difficult to establish the exact timing of sea level events during MIS5e (Rovere et al., 2016). The only way to investigate the evolution of polar meltwater contributions during any interglacial is to obtain a continuous proxy sea-level record from across the interval. So far this has proved elusive from coral reef sites (such as in Dutton et al., 2015; Hibbert et al., 2016).

Coastal strandplain depositional sequences hold the potential to archive such sea-level history at sub-centennial scale resolution (Hein and Ashton, 2020). The process-response drivers of coastal strandplain deposition are relative sea-level, sediment supply and wave energy (Roy et al., 1994; Cowell et al., 2003; Storms et al., 2002). The sediment supply is a function of the alongshore or crosshore transport potential, directional wave climate and in some locations, fluvial discharge (Roy et al., 1994). Fortunately, the strandplains also archive the time-varying shoreline planform geometry that preserve changes in nearshore directional wave climate (direction and spread), that reflect the evolution of ocean wind/wave fields and synoptic circulation (Goodwin et al., 2020). Recent advancements in surface and sub-surface geophysics and in geochronological methods (airborne LiDAR surveys, Optically Stimulated Luminescence (OSL) single grain dating and Ground Penetrating Radar (GPR) surveys) have enabled high spatio-temporal investigations of Holocene coastal strandplain morphology as an integral proxy for relative sea-level history (Tamura, 2012; Costas et al., 2016; Brooke et al., 2019), particularly in far-field settings where GIA regression dominates (Mitrovica and Milne, 2002) and controls accommodation space (Cowell et al., 2003).

However, not all strandplains contain a preserved record of paleoshoreline and RSL. For example, many high-energy coastal strandplains are unsuitable for paleo sea-level reconstruction, since reworking of the depositional signature has been modified by frequent storm wave erosion, cut and fill and/or aeolian reworking (Hein and Ashton, 2020). Instead, prime targets for the preservation of proxy sea-level time series are embayments characterized by low modal wave climate, tide-dominated or modified energy, infrequent storm wave erosion and low wind erosion and reworking (van de Plassche, 1986; Shennan, 2015, after Short, 1999). Additional key criterion are: (i) whether modern and Holocene hydrodynamics and sediment supply are analogous to previous interglacial conditions; and (ii) that neotectonism during the MIS5e interglacial and contamination of the sea-level record fidelity has not occurred. A caveat is that subsequent (post 5e) neotectonism may impact the interpretation of absolute sea-level change but will not affect the internal MIS5e RSL variability (Rovere et al., 2016).

Marginal sea locations offer the most potential for preserving such a continuous relative sea-level record. In the Australian region, northern locations within the Great Barrier Reef lagoon or within the Gulf of Carpentaria where low energy wind waves prevail, offer potential, but are within the impact zone for Tropical Cyclones and hence contain a skewed sedimentary record towards storm event magnitude and frequency (Tamura et al., 2018; Short, 2020). In Southern Australia, the South Australian Gulfs and Bass Strait coasts include suitable tide-dominated and low wave exposure regimes, together with a sand supply (Short, 2006a; b). In this study, we chose to investigate the MIS5e sea-level history from the Bass Strait coast where extensive tide-modified sedimentary coastlines are sheltered from the prevailing SW-W swell direction and not directly exposed to subtropical or extratropical cyclone storm waves (Short, 2006a; and b).

In addition to the suitability of coastal processes and preservation of the morphosedimentary record, the climatological location of the study site is important if we are to assess the paleo RSL with respect to regional climate change. The Bass Strait region straddles the subtropical to mid-latitude boundary and is sensitive to latitudinal shifts in climate boundary conditions (eg. Subtropical ridge (STR, the latitude of the highest mean tropospheric pressure) and storm tracks, Drosdowsky, 2005, Timbal and Drosdowsky, 2012, Goodwin et al., 2016) making it a suitable location for reconstructing weather regime shifts that controlled wind and wave climate during MIS5e (Fig. 1). The reconstructed wind and wave climate provides an important constraint on the regional latitude of the Subtropical Ridge, particularly in the light of future poleward shifts under a warming climate (Lucas et al., 2014).

Previous research has identified morpho-sedimentary evidence for the preservation of MIS5e shorelines around Bass Strait, including field research on rock platforms, estuarine deposits and coastal barriers (Baker and Gill, 1957, Jennings, 1961, Sutherland and Kershaw, 1971; Murray-Wallace and Goede, 1995, Gardner et al., 2008). However, these deposits have only captured a fragmentary record of MIS5e sea levels.

Aerial surveys over Robbins Island in western Bass Strait, off the NW Tasmanian coast, have revealed a potentially extensive late Quaternary strandplain (Van de Geer, 1981; Van de Geer et al., 1979; Bowden and Colhoun, 1984; Murray-Wallace and Goede, 1995) (Fig. 2). This strandplain is known as the Remarkable Banks and is 7 km wide across Robbins Island from White Rock Ridge to the Holocene Barrier (HB) and modern Ransonnet Bay coast. We investigate the Remarkable Banks strandplain evolution, as the index site for MIS5e regional sea-level, wave climate and coastal processes in Bass Strait. We stratigraphically and chronologically tie MIS5e RSL and paleoshoreline data around Bass Strait to produce a regionally-integrated palaeo-sea level signal. Our MIS5e research is underpinned by rigorous evaluation of the modern MetOcean conditions and hydrodynamics (tides, waves, winds, currents and sea-level) in Bass Strait (Mortlock and Goodwin, 2018a,b). This enabled the development and application of a sea-level budget approach by examining the potential impact of changes in wave climate and boundary currents on dynamic sea-level in the Bass Strait region.

1.1. Geographic setting and regional climate of Bass Strait

Bass Strait is a semi-enclosed water body oriented west to east centred on 40°S and separates Tasmania from the Australian mainland. It is a shallow sea with a mean depth of 60 m and mean width of 250 km (Wijeratne et al., 2012). The tidal circulation is mainly semi diurnal, a mesotidal range with the M2 tidal constituent dominating the tides with an amplitude of 0.2–0.4 m at the south-west and south-east entrances, increasing to a maximum of 1.1 m along the central northern Tasmanian coast (Wijeratne et al., 2012). The strongest gradient in tides is experienced along the Tasmania's far northwest shores where the tidal wave becomes substantially amplified over relatively short distances (Donaldson et al., 2012).

At ~40°S, the climate is dominated by the seasonal shift in the position of the subtropical ridge (STR), the location of the highest mean atmospheric pressure, and, to the south, the westerly storm track and frontal mid-latitude lows (Fig. 1). Bass Strait is located at the northern pole of the Southern Annular Mode (SAM) dipole in

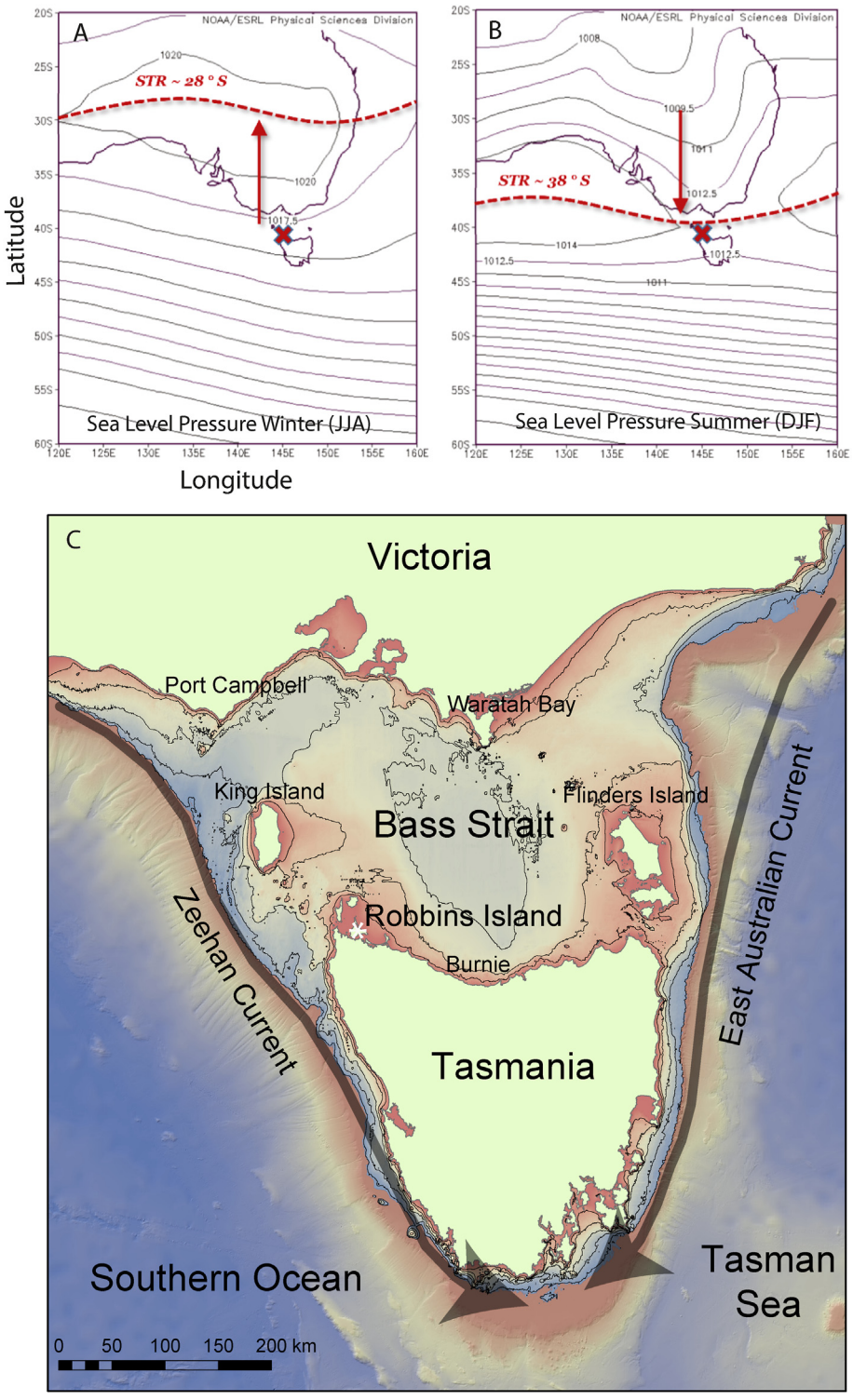

Fig. 1. Location map and seasonal sea-level pressure fields for the Bass Strait region, south-east Australia. (a) sea-level pressure and subtropical ridge (STR) for austral winter; (b) sea-level pressure and subtropical ridge (STR) for austral summer; and (c) bathymetry and topography of the Bass Strait region, and including site locations discussed in text, and major ocean boundary currents.

pressure and latitudinal vacillation of the storm track (after Marshall, 2003; Hemer et al., 2010). The more north westerly storm track controls the seasonal wind and wave climate over northern Tasmania and Bass Strait, that occurs during −ve SAM phases. In summer, the latitude of the STR over Southeast Australia shifts poleward to around 38 °S, a couple of degrees north of Robbins Island (Drosdowsky, 2005). This brings generally more stable weather conditions with more northerly and easterly air flow (Sturman and Tapper, 2006). In winter, the STR shifts equatorward to around 28 °S, drawing the mid-latitude westerlies and Southern Ocean low-pressure systems closer to the Bass Strait region, increasing the prevalence of westerly and south-westerly air flow,

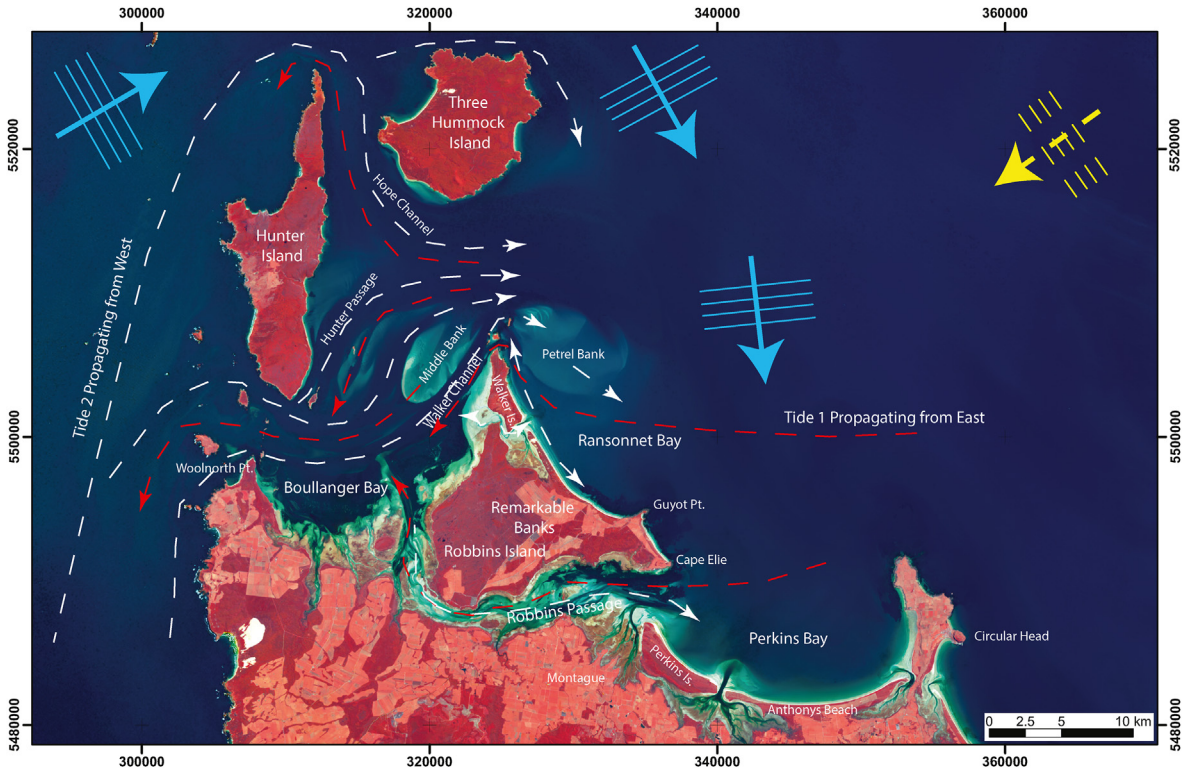

Fig. 2. NW Tasmania satellite image showing marine geomorphic features, islands and key sites discussed in the text, together with tidal currents, shelf sand bodies, and refracted swell directions (westerly and south westerly in blue, easterly and north easterly in yellow).

cold fronts, and associated south-westerly wave energy from higher latitudes in the Southern Ocean (Sturman and Tapper, 2006; Hemer et al., 2010; Goodwin et al., 2016).

The sea-surface temperature and sea-surface height in the Bass Strait region are influenced by seasonal variability of two ocean boundary currents (Cresswell, 2000). In the austral summer, the East Australian Current (western Pacific boundary current) strengthens and causes positive SSTa and SSHa in eastern Bass Strait. In the austral winter, the Zeehan Current strengthens and causes positive SSTa and SSHa in western Bass Strait. The Zeehan Current is the south-eastwards flowing extension of the Leeuwin Current (eastern Indian Ocean boundary current) (Ridgway, 2007) (Fig. 1).

The southern shores of Bass Strait in northern Tasmania are protected from the prevailing energetic westerly swell generated by mid-latitude lows in the Southern Ocean (Short, 2006b). The string of islands from north-west Tasmania (Robbins to Hunter Group to King Island) protect the northwest coast of Tasmania. At the eastern end of Bass Strait the Furneaux Group, Cape Barren Island to Flinders Island, and then the Kent and Hogan Island groups protect the northeast coast of Tasmania. Hence the Tasmanian coast of southern Bass Strait is low-energy, protected from the dominant W-SW swell and is exposed to northerly (NW–N-NE) short-fetch (less than 350 km) wind sea and rarely to short to moderate period easterly cut-off low storm waves generated in the Tasman Sea (Fig. 2) (Porter-Smith et al., 2004; Mortlock and Goodwin, 2018a,b). In contrast, the northern shores of Bass Strait forming the Victorian coast are faced south-east from Cape Otway to Port Phillip Bay and then faced south west to Wilson's Promontory in the east. These northern shores are high energy wave-dominated, open to refracted W-SW Southern Ocean swell and SE Southern Tasman Sea swell (Porter-Smith et al., 2004; Short, 2006a).

1.2. Robbins Island and North-West Tasmanian coast

Robbins Island and Walker Island (40.7 °S, 144.9 °E) are located off the north-western Tasmanian coast, separated from Tasmania by an open tidal channel (Robbins Passage), which at its widest point is 4 km wide (Fig. 2). The regional coastline (extending from Albatross Island to the Circular Head Region) is complex, comprising of: a number of inlets, barrier-lagoons, tombolos and offshore reefs and islands; an extensive network of tidal channels, and intertidal and shallow subtidal flats that are interspersed with seagrass beds (after Mount et al., 2010).

The geology of southwestern Bass Strait and northwestern Tasmania was described by Everard et al. (1997). Underlying most of the region is deformed Mesoproterozoic, dominantly the siliciclastic shelf sequence (Rocky Cape Group) and correlates with orthoquartzite, disconformably overlain by a Neoproterozoic sequence (Togari Group) of dominantly dolomite with a middle interval of basalt, and mudstone/siltstone. Tertiary basalts and related pyroclastic rocks outcrop along the coast. Almost the entire coastal plain from Stanley to Woolnorth Point is overlain by a thick sheet of Pleistocene coastal sand and gravel deposits up to ~20 m above MSL, that grade seawards to paleo-estuarine deposits and a topography indicative of an emergent distributary tidal flat.

Robbins Island consists of two bedrock blocks: the central 50–60 m high White Rock Ridge of the Precambrian Rocky Cape and Togari Groups, and The Bluff which is formed from Tertiary age basalts. These outcrops are tied by coastal strand-plains that have formed during the late Quaternary. The Remarkable Banks

strandplain forms the central portion of the island. A 9 km long outer sand barrier extends from The Bluff along the northeast coast of Robbins Island to Walker Island, an adjoining island to the north. Robbins and Walker Islands are separated by a 300 m wide tidal channel and are located onshore from the inner shoreface sand body known as the Petrel Bank in western Bass Strait.

2. Methods

2.1. Metocean data analysis

Reconstructing past sea-level and wave climate including ocean current influences, requires an understanding of modern wave, current, tidal and sediment transport fields. The caveat is that these are guide only and we sought to understand the modern seasonality to underpin Quaternary sea level reconstruction. We applied high spatial resolution hydrodynamic modelling of wave, current, tidal and sediment transport fields, using instrumental data time-series to the western Bass Strait region. These data were collected as part of the Robbins Island Renewable Energy Park project and made available to the present study (Mortlock and Goodwin, 2018a,b). The modern climate and hydrodynamic data are summarised below and in detail in Mortlock and Goodwin (2018a,b).

2.1.1. Tide and relative sea level data

Water level observations made in Robbins Passage and Boullanger Bay by Donaldson et al. (2012) were obtained for this study and used as a calibration dataset for the model and to form a conceptual understanding of the hydrodynamics of the area. The nearest, long-term sea level record to the study site is at Burnie, approx. 90 km to the east of Robbins Island. Continuous sea level measurements have been undertaken at this site since 1952. From 1952 to 1991, data was collected by Burnie Port Authority. Since 1992, data has been collected by the National Tide Centre and forms part of the Australian Baseline Sea Level Monitoring Project.

The hourly record from September 1992 to April 2018 (~26.6 years) was obtained from the Australian Baseline Sea Level Monitoring Project through the BoM. Data was converted from the local Chart Datum to AHD. Data was provided relative to AEST. In addition to sea level, this dataset includes: water temperature, air temperature, barometric pressure, sea level residuals, sea level anomalies, and wind speed, gusts and direction. In addition, the monthly sea levels from July 1952 to February 2018 (~65.4 years) were obtained from the National Tide Centre via the Permanent Service for Mean Sea Level (PSMSL). Data includes minimum, maximum, mean and standard deviation of monthly sea levels. Data was converted from the local Chart Datum to AHD.

2.1.2. Wind data

Wind observations were sourced from; Cape Grim ((40.6828 °S, 144.69 °E, station no. 091245, BOM), approx. 20 km east of Robbins Island; Smithton Aerodrome (40.8347 °S, 145.0847 °E, station no. 091292, BOM), approx. 25 km south-east of Robbins Island; and on Robbins Island itself. Observations from Wynard Airport (BOM), approx. 100 km east of Robbins Island, were also analysed.

2.1.3. Wave buoy data

Instrumental ocean wave data were available for: (i) Cape Sorrell wave buoy off the Tasmanian west coast (42°9.0′S, 145°1.0′E, 100 m depth, over 150 km to the south of Robbins Island on the continental shelf off the west coast of Tasmania, but indicative of the swell wave climate for the west coast Tasmanian continental shelf, and particularly the SW and W swell, that propagates into western Bass Strait, Hemer et al., 2010); and (ii) short-term wave buoy data from Cape Grim between March 1991 and April 1992 (~1.1 year) (65 m water depth 15 km off the north-west coast of Tasmania 40.78 °S, 144.55 °E. Reid and Fandry, 1994).

2.1.4. The CAWCR wave hindcast data

In the absence of long-term wave observations for western Bass Strait and the Robbins Island region, our wave climate analysis was based on hindcast (modelled) wave parametric data from CSIRO's CAWCR (Centre for Australian Weather and Climate Research) wave hindcast (Durrant et al., 2014). CAWCR represented the best-resolution hindcast wave data available (at the time of analysis) for Australian shelf waters. The CAWCR wave hindcast covers a 36-year period from 1979 to 2014 providing hourly data at a global scale with a resolution of 0.4° (Durrant et al., 2014). Additionally, several nested grids (including Bass Strait) provide data at a resolution of 4' (approx. 7 km). The hindcast wave model uses WAVEWATCH III v.4.18 with a mosaic grid method where grids of differing resolution are run concurrently (Durrant et al., 2014). Subsequent to our analysis a new wave hindcast modelling experiment was undertaken by Liu et al. (2022) that yields comparable results.

2.1.5. Hydrodynamic modelling

We ran high-spatial resolution hydrodynamic modelling under idealised wave and wind scenarios to produce wave transformation output for direct comparison to the paleo-shoreline geometry and to model currents and sediment transport. This enabled attribution of paleo-wave climate and current fields to the geohistorical record. We applied the MIKE 21 suite of models developed by the Danish Hydraulic Institute (DHI (2016) and used high-resolution LiDAR bathymetries (see below). This is discussed in detail in Mortlock and Goodwin (2018a,b). A spectral wave model was coupled to a hydrodynamic flow model and a sediment transport model to simulate wave growth, wind- and wave-driven set up, wind- and wave-driven currents, sediment transport and morphological change in Robbins Passage and on the east coast of Robbins Island. The modelling scenarios were developed from the analysis of the modern wave climate data from buoys and CAWCR hindcasts. We used tidal data from Donaldson et al. (2012) and calibrated the tidal current flow fields against these observations.

2.2. LiDAR survey and DEM of terrestrial topography and marine bathymetry

Four different bathymetric sources were used. A Riegl VQ820G Topo-Hydrographic LiDAR systems mounted in underwing pods on a Dimona (HK36TTC-ECO) motorglider-based research aircraft. Flying height was conducted at 600 m amsl with point densities between 10 and 12 points/m^2. The LiDAR point cloud elevation was referenced to the Australian Height Datum (AHD) and was processed using the LAStools® (rapidlasso.com version 1.3) and BayesMap® Stripalign (version 1.6) to correct both relative and absolute geometric errors. The DEM was generated using the GlobalMapper® LiDAR module (version 19) "binning" process searching for the minimum values. The DEM was exported as a 0.5 m DEM. The multi-sensor airborne topographic and bathymetric LiDAR system was able to capture elevations from 71 m to −15 m AHD, covering all of the inter- and sub-tidal morphology in Robbins Passage and a good portion of the subaqueous upper shoreface around Robbins and Walker Islands. In addition, the east coast of King Island was also surveyed by the LiDAR system. Reported vertical accuracy (to one RMSE, or 68% confidence) is ±0.15 m. (surveys flown by Airborne Research Australia, J. Hacker, pers. Comm., 2016).

This data were complemented by another LiDAR-derived DEM collected as part of the state-wide Climate Futures for Tasmania (CFT) project, completed in 2008 (climatefutures.org.au). This

covered the mainland Circular Head coastline and parts of Boullanger Bay not captured by the Airborne Research Australia LiDAR. The CFT LiDAR extends from the low water mark to 40 m in depth or 1.5 kms from the shore (whichever boundary is first encountered). Proximal to Robbins Island, the depths extended to − 10 m AHD (Australian Height Datum). The DEM was available at a one square-metre resolution. The reported vertical accuracy (to one RMSE) is ±0.25 m. For all other areas in the model domain not covered by the above two LiDAR datasets (generally, elevations < - 10 m AHD), soundings and contour lines were digitized from Australian Hydrographic Office (AHO) nautical chart AUS 790 Stokes Point to Rocky Cape, Nov 2004 edition. Contour lines were converted to points equally spaced at 0.005° intervals. Depths were converted to elevations, with respect to Chart Datum and then to AHD (−2.06 m).

Desktop surveys using the new LiDAR DEM flown for this study were conducted for Robbins Island and King Island, and using existing LiDAR data for Port Campbell and Waratah Bay (discover.data.vic.gov.au), and SRTM data for Flinders Island (ga.gov.au).

2.3. Field sampling: GPR stratigraphy and geochronology

Detailed field surveys were conducted around the entire Robbins and Walker Islands, Montague to Circular Head coast, NW Tasmania. Additional field surveys were conducted on Flinders Island and along the Otway coast from Port Campbell to Peterborough. All sediment sample descriptions and interpretations in the text are based upon field measurements and stratigraphic analysis. Quantitative sediment size analysis was not undertaken for this study.

Subsurface investigations were completed using GPR surveys and pit excavations. The GPR surveys were conducted over the Remarkable Banks strandplain using a Sensors and Software Pulse EKHO GPR transceiver and 250 and 500 MHz antennae. GPR imagery was obtained for the sand profile above the water table. All GPR data was gained with DEWOW filter, corrected for time zero, and minimal post-processing using only low pass spatial and migration filters using a velocity of −0.149 m/s as determined from depth-velocity calibration in pit excavations.

The surface topographic profiles were obtained using differential GPS surveys combined with LiDAR DEM data. Sub-surface stratigraphy and sediment samples were obtained for OSL dating using shallow pits (~1 m deep), 6 m depth auger hole techniques and 3 m deep open pits exposed by a mechanical excavator. The augering and excavations were completed to below the water table. Note that recovery from augers in swales along the central part of the Remarkable Banks was poor due to the high water table and no OSL ages were obtained.

The planform geometry for the paleo shoreline discontinuities and morphometrics were extracted graphically from the DEM's in a GIS framework and mapped together with the modern shoreline geometry. We applied the sequence stratigraphy approach, normally used to interpret geological vertical sections, to transfer the horizontal 2-D stratigraphy of temporally-consistent sequences of coastline planform geometry between nearby coastal compartments (Goodwin et al., 2020). We refer to this as 'Coastal Planform Sequence Stratigraphy'. This ensemble approach ensures that we obtain replicated planform discontinuities that represent a sub-centennial scale integration of wave climate variability and are not a function of autogenic processes for independent emabyments.

The sequence of coastal evolution was constrained by both radiocarbon age determination and optically stimulated luminescence (OSL) methods. Radiocarbon ^{14}C age determination was applied to shell samples collected from auger holes and excavated pits. Most of the ^{14}C age were determined by AMS techniques at BETA Analytic, and were calibrated to calendar ages with a 2 sigma error range. OSL dating was conducted in two laboratories (TRAPS-Macquarie University and University of Gloucestershire). Opaque tubes hammered into cleaned sections of pits and the base of auger holes were utilized to collect sediment for luminescence dating. Quartz grains of 180–212 μm diameter were separated from the matrix under dim red illumination using standard purification procedures, including a final etch in 40% hydrofluoric acid for 45 min to remove the external alpha-dosed rinds (Aitken, 1998). Here we used single-grain optically stimulated luminescence (OSL) techniques using UV emissions with a modified SAR protocol (Murray and Wintle, 2000) for ~1000 single-grains loaded on aluminium single-grain discs. Concentrations of 238U, 235U, 232 Th (and their decay products) and 40 K were measured by Geiger-Muller multi-counter beta counting of dried and powdered sediment samples in the laboratory and via in situ measurements using a portable gamma spectrometer in the field.

Field moisture content was measured on all samples in the laboratory and a moisture content-depth curve was determined to assign an approximation for the long-term average moisture content. The latter is a vexed issue over Late Quaternary time scales due to the numerous climate shifts. A major assumption in our calculations is that the low slope across the Remarkable Banks and the dune swale topography have maintained moisture profiles and poor drainage similar to modern under persistent rainfall from mid-latitude storm tracks. Last glacial peat deposits now exposed in Robbins Passage attest to poor drainage. Consequently, field moisture contents for the sub-surface OSL samples produced stratigraphically consistent ages clustered within MIS5e. Depth of overburden was measured from the surface, and since there has been only a single depositional event, these depths were applied to the age determination calculations. All ^{14} C radiocarbon and OSL ages are listed in Tables 1–4. For OSL ages we include both Central Age Model (CAM) and Mininimum Age Model (MAM) where the samples showed a degree of overdispersion or more than one population of grains (typically samples that contain MIS7 and MIS5e age grains).

2.4. Paleo sea level indicator calibration to modern sea level

Two morphological features were used as paleo sea-level indicators across the Remarkable Banks: (i) top of intertidal welded nearshore surf-zone bar; and (ii) interface between laminated beachface and overlying cap of aeolian cross-bedded foredune sand. In addition, ancilliary data from an emergent boulder beach berm and limit of runup and emergent rock platform surface elevation at Guyot Point, Robbins Island were examined. The elevation range of the modern analogues for paleo sea-level indicators was determined by dGPS survey relative the local tidal plane range to give an indicative range. The paleo beachface and intertidal bar sea-level indicators were identified within pits and the adjacent depth-calibrated GPR radargrams. The spatial variability of all indicators was assessed using the high resolution DEM's.

2.5. Paleo wave direction reconstruction

Time-varying wave direction has the potential to influence RSL at the shoreline through changes in incident wave power and sediment transport. The parabolic curvature of each of the ridges forming the strandplains robustly defines the nearshore wave refraction pattern of the shoreline during deposition (Davies, 1972; Hsu and Evans, 1989; Hsu et al., 2010). The shoreline planform geometry (curvature, indentation, orientation) together with the

Table 1
OSL ages of sand samples from Robbins Island and Walker Island.

Sample	Latitude° S	Longitude° E	Elevation (m)	Overburden (m)	Moisture Content (%)	Dose Rate (Gy/Ka)	Paleodose (Gys)	OD (%)	Model	Age (ka) BP
RemB01/17	−40.71364	144.91946	11.16	4.5	34	0.623 ± 0.044	81.2 ± 2.47	32.6	CAM	130.3 ± 10.1
RemB01/17	−40.71364	144.91946	11.16	4.5	34	0.623 ± 0.044	81.2 ± 2.47		FMM	84.7 ± 6.3
RemB01/17	−40.71364	144.91946	11.16	4.5	34	0.623 ± 0.044	81.2 ± 2.47		FMM	136.3 ± 9.9
RemB01/17	−40.71364	144.91946	11.16	4.5	34	0.623 ± 0.044	81.2 ± 2.47		FMM	193.4 ± 14.5
RemB02/17	−40.67417	144.95735	6.25	1.1	12	0.297 ± 0.031	35.84 ± 1.11	28.5	CAM	120.5 ± 13
RemB03/17	−40.67417	144.95735	6.78	1.2	20	0.299 ± 0.031	36.28 ± 0.92	20	CAM	121.3 ± 13.7
RemB03P1/18	−40.67417	144.95735	6.78	2.35	22	0.366 ± 0.034	44.96 ± 1.42	27.5	CAM	122.9 ± 12.1
RemB03P2/18	−40.67417	144.95735	6.78	2.1	8	0.396 ± 0.063	51.31 ± 1.86	30.6	CAM	129.5 ± 21.2
RemB03P3/18	−40.67417	144.95735	6.78	1.75	22	0.373 ± 0.062	45.58 ± 1.4	25.4	CAM	122.3 ± 20.8
RemB04/17	−40.67534	144.95566	6.783	1.2	3	0.282 ± 0.030	34.31 ± 1.00	27.3	CAM	121.8 ± 13.6
RemB06/17	−40.67209	144.96058	6.34	1.2	17	0.282 ± 0.030	36.62	18.0	CAM	119.1 ± 14
RemB15P1/18	−40.67209	144.96058	5.33	2.8	30	0.363 ± 0,050	43.84 ± 1.85	34.0	CAM	120.7 ± 17.5
RemB15P3/18	−40.67209	144.96058	5.33	1.8	25	0.341 ± 0.039	48.43 ± 1.69	24.9	CAM	141.9 ± 16.9
RemB16P1/18	−40.67142	144.96172	5.1	1.6	17	0.373 ± 0.045	44.81 ± 1.53	28.3	CAM	120.2 ± 15.1
RemB07/17	−40.66941	144.96359	4.996	1.2	19	0.304 ± 0.029	35.96 ± 1.15	23.1	CAM	118.2 ± 11.8
RemB08/17	−40.66941	144.96359	4.996	1.0	7	0.297 ± 0.030	34.53 ± 1.09	23.9	CAM	116.1 ± 12.3
RemB09/17	−40.66658	144.96661	3.875	1.5	22	0.244 ± 0.024	28.74 ± 0.60	16.6	CAM	117.7 ± 11.9
RemB010/17	−40.66286	144.96199	3.296	1.6	7	0.389 ± 0.041	45.7 ± 1.36	25.9	CAM	117.5 ± 12.7
RemB011/17	−40.68619	144.96528	10.432	2.0	10	0.564 ± 0.049	10.79 ± 0.38	27.3	CAM	19.1 ± 1.8
RemB012/17	−40.68552	144.98619	5.031	1.2	20	0.316 ± 0.032	37.18 ± 3.05	80.9	CAM	117.6 ± 15.2
RemB012/17	−40.68552	144.98619	5.031	1.2	20	0.316 ± 0.032	37.18 ± 3.05	80.9	FMM	15.4 ± 1.6
RiHBN02/17	−40.67101	144.98597	5.201	0.5	10	0.517 ± 0.043	1.45 ± 0.07	38.4	CAM	2.8 ± 0.3
RiHBN02/17	−40.67101	144.98597	5.201	0.5	10	0.517 ± 0.043	1.45 ± 0.07	38.4	FMM	2.1 ± 0.6
RiHBN02/17	−40.67101	144.98597	5.201	0.5	10	0.517 ± 0.043	1.45 ± 0.07	38.4	FMM	4.7 ± 1.6
RiHBN03/17	40.67000	145.00000	9	0.9	10	0.435 ± 0.037	0.77 ± 0.03	25.7	CAM	1.8 ± 0.2
RiGP02/17	−40.66667	145.04514	5.341	0.5	3	0.328 ± 0.034	6.36 ± 0.24	42.9	CAM	18.1 ± 2
RiGP02/19	−40.66667	145.04588	5	0.75	20	0.362 ± 0.032	5.56 ± 0.14	32.4	CAM	16.7 ± 1.5
Mos01/19	−40.61733	144.92859	5	4.20	5	0.335 ± 0.029	7.64 ± 0.16	26.8	CAM	22.8 ± 2
Mos02/19	−40.61908	144.93917	3.5	2.55	3	0.282 ± 0.025	7.17 ± 0.14	21.5	CAM	25.4 ± 2.3
Mos03/19	−40.61502	144.93917	3.4	2.10	2	0.314 ± 0.025	7.51 ± 0.18	18.6	CAM	23.9 ± 2
Wal01/19	−40.6357	144.93289	5	2.60	2	0.407 ± 0.035	0.84 ± 0.02	16.2	CAM	2.1 ± 0.2
Wal02/19	−40.63925	144.93289	4.8	0.65	5	0.629 ± 0.048	3.49 ± 0.08	96.5	FMM	5.5 ± 0.4
Wal03/19	−40.63925	144.93289	4.8	0.80	5	0.362 ± 0.032	1.56 ± 0.06	36.0	CAM	4.3 ± 0.4

Table 2
OSL ages of sand samples from Anthonys beach.

Sample	Latitude ° S	Longitude ° E	Elevation (m)	Overburden (m)	Moisture Content (%)	Dose Rate (Gy/Ka)	Paleodose (Gys)	Overdispersion (%)	Model	Age (Ka)
AB01/16	−40.8086	145.1877	5.374	1.55	2	0.42 ± 0.06	1.2 ± 0.1		MAM	2.9 ± 0.5
AB02/16	−40.81404	145.1880	3.821	0.8	2	0.35 ± 0.08	2.1 ± 0.2		MAM	6 ± 2
AB04/17	−40.80498	145.1833	5.6	0.7	3	0.421 ± 0.032	0.47 ± 0.02	30.5	CAM	1.1 ± 0.1
AB04/17	−40.80498	145.1877	5.6	0.7	3	0.421 ± 0.032	0.47 ± 0.02	30.5	MAM	0.83 ± 0.08
AB05/17	−40.80441	145.1877	~5	1.0	3	0.439 ± 0.031	0.27 ± 0.02	47.3	CAM	0.6 ± 0.1
AB05/17	−40.80441	145.1877	~5	1.0	3	0.439 ± 0.031	0.27 ± 0.02	47.3	MAM	0.4 ± 0.06
AB06/17	−40.80422	145.1877	0.56 m	2.2 m	3	0.445 ± 0.031	0.16 ± 0.02	62.3	CAM	0.4 ± 0.01
AB06/17	−40.80422	145.1877	0.56 m	2.2 m	3	0.445 ± 0.031	0.16 ± 0.02	62.3	MAM	0.17 ± 0.03

Table 3
OSL ages of sand samples from Flinders island.

Sample	Latitude °S	Longitude °E	Elevation (m)	Overburden (m)	Moisture Content (%)	Dose Rate (Gy/Ka)	Paleodose (Gys)	OD (%)	Model	Age (Ka) BP
FiNER 0IF/16	−39.72083	147.9525	5.4	1	2	0.95 ± 0.06	116 ± 5		CAM	123 ± 10
FilNER 01 B/16	−39.72083	147.9525	3.65	2	2	0.96 ± 0.04	121 ± 6		CAM	127 ± 9

Table 4
AMS radiocarbon ages.

Sample	Material	Latitude °S	Longitude °E	Elevation (m)	Depth (m)	% Modern Carbon	Conventional 14C Age (yrs Before, 1950)	Calibrated 14C Age (Calendar yrs Before, 1950)	Lab Sample Code
Robbins Island and Walkers Island									
RiBLF01/17	Shell	−40.68537	145.0253	3.08	0.5	83.80 ± 0.31	1420 ± 30	1064-741 cal BP	Beta 483,638
RiHBN02/17	Shell	40.67101	144.98597	5.201	0.5	1.70 ± 0.04	32,720 ± 180	36,575-35,690 cal BP	Beta-483637
Wal02/19	Shell	−40.63925	144.9496	4.8	0.65	1.15 ± 0.04	35,860 ± 260	40,671-39,301 cal BP	Beta 529808
Port Campbell									
PC01/19	Shell	−38.62472	142.9708	2.2	0.1	63.09 ± 0.24	3700 ± 30	3726-3370 cal BP	Beta-529809

dominant or resultant nearshore MWD was reconstructed using simple graphical techniques such as those utilized in the MetBay approach (Klein et al., 2003). The associated deepwater paleoMWD for each planform was reconstructed using back trajectory (or inverse modelling) analysis of wave rays using: (i) the modelled nearshore refraction pattern of wave rays output from Mike21 hydrodynamic modelling for a range of parametric wave cases (E through to W MWD); and, (ii) the radiating great circle paths from the Bass Strait shorelines back to the respective wave generation source regions: proximal within Bass Strait; and distal in the Tasman Sea and the Southern Ocean.

2.6. GIA modelling and RSL time series

We modelled the Glacio-Isostatic Adjustment (GIA) for Robbins Island and the other Bass Strait sites. We applied one-dimensional Maxwell viscoelastic Earth models defined by constant upper (ν_{UM}) and lower mantle viscosities (ν_{LM}), which we vary as free parameters. A full description of the GIA modelling approach based on a pseudo-spectral algorithm for solving the sea level equation is found in Kendall et al. (2005). Our calculations adopt a spherical harmonic decomposition at degree and order 256, and implement rotational feedback into the predictions using the stability theory of Mitrovica et al. (2005). Lithospheric thickness of ~50 km under Bass Strait is suggested from published seismic observations of the Australian lithosphere (Simons and van der Hilst, 2002) and by Richards et al. (2002) and Hoggard et al. (2020) in an analysis of geophysical observations and laboratory mineral physics observations. The model described in the latter two studies also suggests (logarithmic) average viscosities of ~0.5×10^{21} Pa s in the upper mantle and ~5×10^{22} Pa s in the lower mantle. We adopt these values in the main results below, but also applied sensitivity testing of our results to a wide range of other values for ν_{UM} and ν_{LM} to produce an envelope of Relative Sea Level (RSL) solutions. We adopt the I_{LAM} ice history of Dendy et al. (2017), as refined by Clark et al. (2020). For all times prior to the LGM, the GMSL curve of the I_{LAM} model follows the timing and magnitude of the SL curve of Waelbroeck et al. (2002) and, with one exception, we assume that ice geometries pre-LGM are identical to those post-LGM whenever global mean sea level values match. The exception is the passage into and out of the Penultimate Glacial Maximum (PGM). In this case, I_{LAM} adopts the Lambeck et al. (2006) ice model at the PGM in which, in contrast to the LGM, Eurasian ice volume is comparable to North American ice volume.

3. NW Tasmania Metocean, wind, waves, coastal currents and sand supply

3.1. Winds

The wind climate comprises of an Easterly, (30–150°), a Southwesterly (150–320°), and a Northerly mode (320–30°). The prevailing wind direction is the southwesterly, although strong winds (>15 m/s, or 29 knots) can occur less frequently from both the E and N sectors. The wind rose for the 2003–2008 U10 wind climate is shown in Fig. 3a. A seasonal break down of the three directional sectors shows that SW winds are relatively constant year-round and make up the bulk (approx. 62%) of the annual wind climate. Seasonal variations occur between the relative occurrence of N and E winds due to the seasonal latitudinal shift in the STR.

3.2. Waves

The modern Robbins Island regional wave climate is associated with the following weather regimes: (i) Southern Ocean, mid-latitude Low forced southwesterly (SW) wave train refraction clockwise around Hunter Island and into shallow Bass Strait water; (ii) Westerly (W) winds and swell waves from cut-off lows in the Great Australian Bight and from embedded cold fronts as the cut-off lows migrate through Bass Strait;
(iii) NE wind sea from frequent anticyclonic winds and less frequent mesoscale lows in eastern Bass Strait; (iv) Infrequent NE long-period swell waves from Central Tasman Lows, and/or Tropical Lows, propagating through an acute swell window of 55–70° MWD between Wilsons Promontory and Flinders Island; and,
(v) Strong SW winds create cross-offshore directed waves and bi-directional wave conditions to the east of Robbins Island (Mortlock and Goodwin, 2018a,b). We assess the MIS5e wave climate as a departure from the modern in section xx and discuss any implications for the interpretation of local RSL history.

The sheltered Robbins Island and NW Tasmanian Islands are exposed to refracted Southern Ocean swell from the SW (220–250°), and W (260–270°) at the western opening of Bass Strait (see Fig. 2 and wave rose for the Ransonnet Bay coast, Robbins Island in Fig. 3b). Eastern Bass Strait and the configuration of islands, particularly Flinders Island, limit the swell window from Tasman Sea generated waves to be ENE (55–70°), allowing the propagation of storm waves from Central Tasman Lows. All other incident waves with directions ranging from NW to E (300–80°) are fetch-limited short-period waves and wind sea, with a maximum fetch length of about 350 km. These propagate to the Ransonnet Bay and Perkins Bay coast primarily from eastern Bass Strait, and to a lesser extent, northern Bass Strait (Fig. 2).

Hence, the wave climate offshore to the north and east of Robbins Island is bimodal with a NE wind-sea and swell mode (MWD of 68°, Hs, 1.3 m, Tp 6.0 s) and a W mode (MWD of 262°, Hs, 1.1 m, Tp 8.4 s) that is the Southern Ocean swell refraction to the north of Three Hummock Island. The resulting bimodal wave climate incident at the Ransonnet Bay coast shoreline (NE facing Robbins Island), comprises; (i) low energy W mode swell, with a modal Hs of 0.4 m, modal mean wave direction (MWD) of ~N (modal MWD 9°) and a Tp of 4.6 s; and (ii) NE-E fetch-limited wind-sea waves with small modal Hs 0.4 m, modal Tp 4.7 s and a modal 50° or 53° MWD. Waves from the N have very small wave height (most common is 0.1 m), and short period (4.6 s, similar to NE waves) from local wind generation. However, the wave data suggests waves of over 2 m, are possible from the N during extreme wind conditions, and from NE swell propagating into eastern Bass Strait from the Tasman Sea. Almost all other waves are offshore propagating between S to W wind sea driven by the prevailing S, SW and W winds, that comprise of 50% of the annual wave climate.

Overall, the wave analysis shows that there is a subtle 5° MWD shift between refracted SW swell waves (a refracted MWD of 9°) and E wind-driven seas (observed as NE short period waves), which is distinguished in DJF (58° MWD) from all other seasons (53° MWD). A poleward STR (modern DJF) produces ~ N modal wave climate and an equatorward STR (modern JJA) produces a ~NE modal wave climate along the Ransonnett Bay and Perkins Bay coast.

3.3. Relative sea-level variability

Over the past ~65 years, the highest maximum and lowest minimum tidal-forced, monthly sea levels have varied from 2.01 m above AHD (37 cm above HAT) to −2.37 m below AHD (47 cm below LAT). Monthly sea level residuals of ±0.2 m occur due to climate forced dynamic and barometric sea-level components range in association with ENSO and/or SAM (Pariwono et al., 1986; White et al., 2014). The largest three storm surge events at Burnie since 1992 were all produced by the passage of westerly to north-

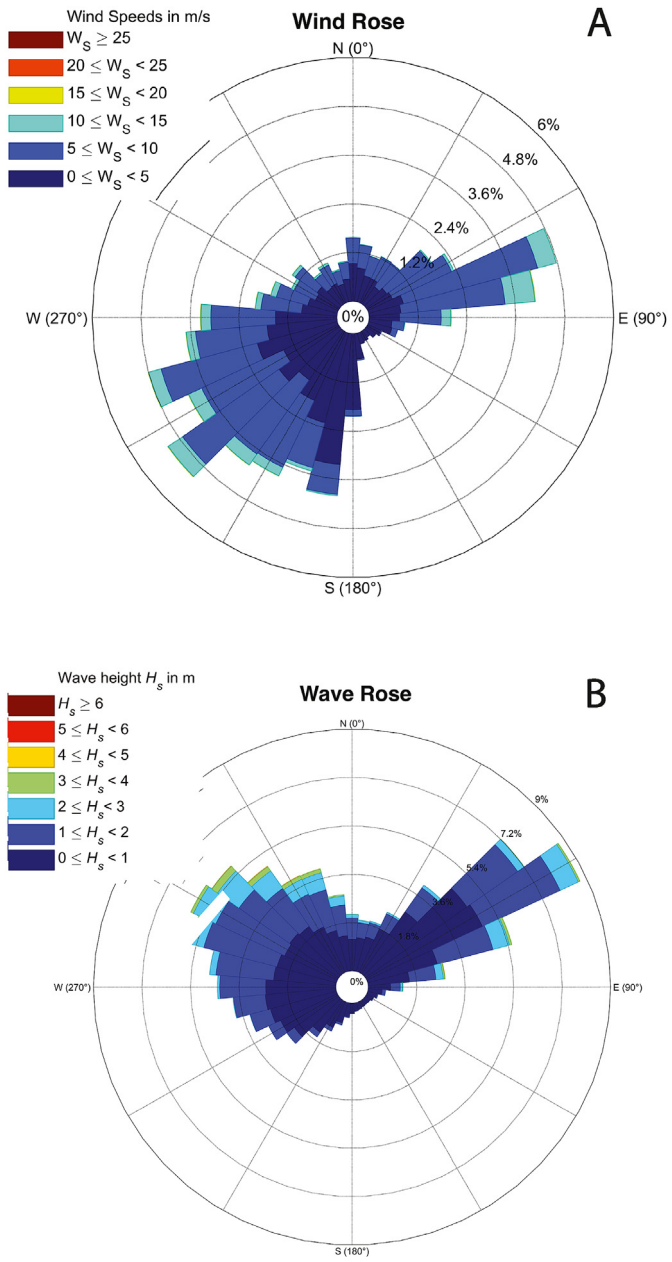

Fig. 3. Directional Wind and Wave Climate at Robbins Island: (a) Directional wind climate at Robbins Islands; (b) Directional wave climate offshore in Ransonnet Bay at ~30 m water depth.

westerly frontal winds through Bass Strait. Studies by McInnes and Hubbert (2003), McInnes et al. (2009) and O'Grady and McInnes (2010) showed that approx. 80% of cases of elevated sea level events in Bass Strait are produced by cold fronts. However, while Burnie may be exposed to both westerly and easterly surge events, Robbins Passage and the coast of Robbins Island are only vulnerable to (less common) easterly surge events, being largely sheltered from winds and waves from the west.

3.4. Robbins Island to Perkins Bay coast hydrodynamics

Our study of NW Tasmania also includes the coastal barrier evolution from Robbins Island east, including Montagu, Smithton, Perkins Island and alongshore Anthony's Beach to Circular Head. The modern coast, bathymetry, MWD and currents from Hunter Island to Circular Head and Stanley is shown in Fig. 2. Robbins Passage is an east-west oriented tidal channel, spanning an area of approx. 60 square kilometres. This can be broadly separated into two geographic regions; Robbins Passage East and Robbins Passage West (Donaldson et al., 2012). The tidal flow is influenced by two main tidal channels that are separated by a low-tide exposed flood ramp at Robbins Crossing. The primary flood tide enters from the east and bifurcates at the eastern entrance to Robbins Passage. One tidal wave propagates through Robbins Passage from the east, while the other travels round the tip of Walker Island via Boulanger Bay in the west. The two tides meet around Robbins Crossing. A second flood tide enters through the passage between Hunter Island and Woolnorth Point. The largest astronomical tidal range decreases from the east to the west, from approx. 3.2 m at Howie Island to 2.4 m at Welcome Inlet, consistent with the regional gradient experienced across northwest Tasmania. Mean spring and neap tidal range varies east to west from 2.8 m to 2.1 m, and 1.8 m–1.3 m, respectively (Mortlock and Goodwin, 2018a,b).

To support out paleo investigations on Remakable Banks, our Mike21 scenario modelling applied the modern wave climate at the wave-break point in Ransonnet Bay as: (i) W or SW swell with a period Tp 8.3 s and a MWD 9°; (ii) NE wind sea and/or swell with a period Tp 7.4 s, MWD 42°; and, (iii) E wind sea with a period Tp 7.0 s, MWD 69°. The modelled wave transformation fields for W and NE modal waves are shown in Fig. 4a,b. The modelled tidal flow fields for flood and ebb tides are along the Walker Island to Robbins Is coast are shown in Fig. 5a,b.

Most of the W wave energy is dissipated on the shallow shoreface or propagates south-eastward (offshore). The offshore propagation of W wave energy is enhanced by strong W winds. Therefore, there is very little wave energy during W modal conditions to drive sediment transport, and the nearshore flow field is principally controlled by tide. Under W wave energy, the tidal asymmetry drives a net southward current during the flood tide. During storm wave conditions from the W the increase in wave power over-rides the underlying tidal current and results in a southward alongshore current.

Model runs indicate that NE waves and winds produce stronger nearshore wave power than W conditions. This is despite the offshore deepwater waves being significantly smaller during NE conditions. For example, modal waves from NE have a deepwater $H_s$of 0.5 m and a $T_p$of 5.1s, whereas modal waves from the W have a deepwater $H_s$of 2.2 m and a T_p of 10.6s but become highly refracted and shoaled when crossing the shoreface with an H_s of 0.5 m and T_p of 10.6s.

NE waves approach broadly perpendicular to the east coast with less energy dissipation than W waves. Hence, the amount of nearshore wave power is higher than during W conditions, and NE waves either enhance a northward alongshore flow (0.2–0.4 m/s), during an incoming tide or oppose and complicate the nearshore flow field during an outgoing tide (an alongshore current of 0.2–0.3 m/s). This suggests the nearshore current field on the Ransonnett Bay coast of Robbins Island is bi-directional and sensitive to wave/wind direction and tidal state. N to NE waves are the principle drivers of shoreward sand transport to the modern coast and to the embayed Remarkable Banks coast during MIS5e, as discussed later in the paper.

3.5. Modern sand supply to the Robbins Island to Perkins Bay coast

In Bass Strait, the predominant sand supply sources are the Quaternary palimpsest deposits comprised of quartzose sand, relict Pleistocene carbonate particles, and abundant Holocene biogenic carbonate (James et al., 2004). The sand supply to Robbins Island is

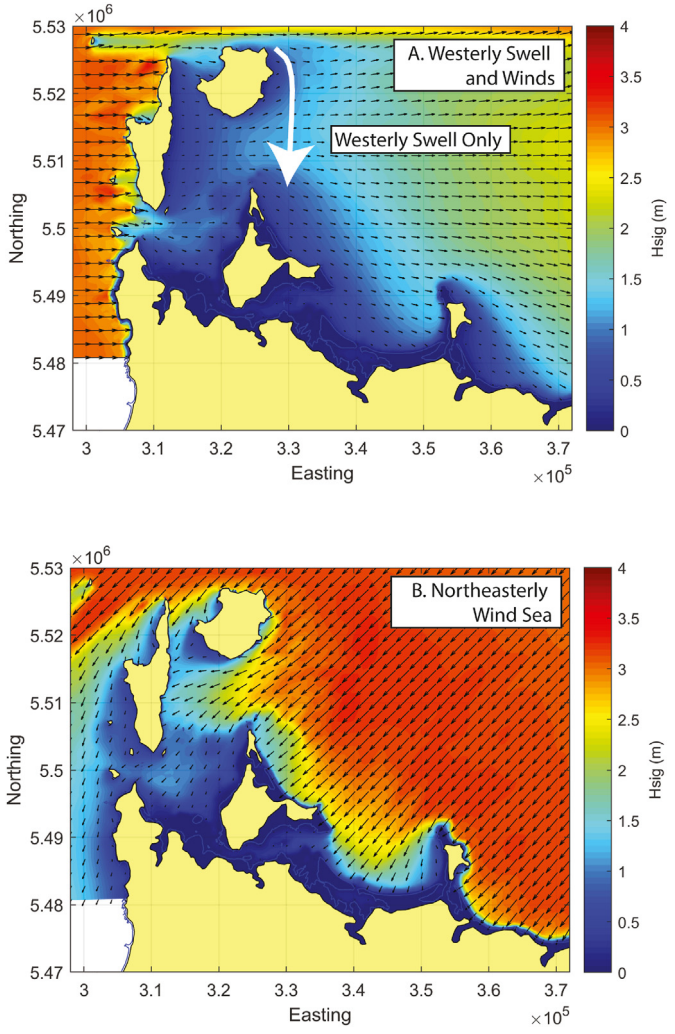

Fig. 4. Modelled modern wave refraction fields for (a) W swell wave direction; and (b) NE wind waves, along the Ransonnet Bay coast of Robbins Island and Walker Island. The water domain has been extended to +5 m to approximate the mid MIS5e coastline.

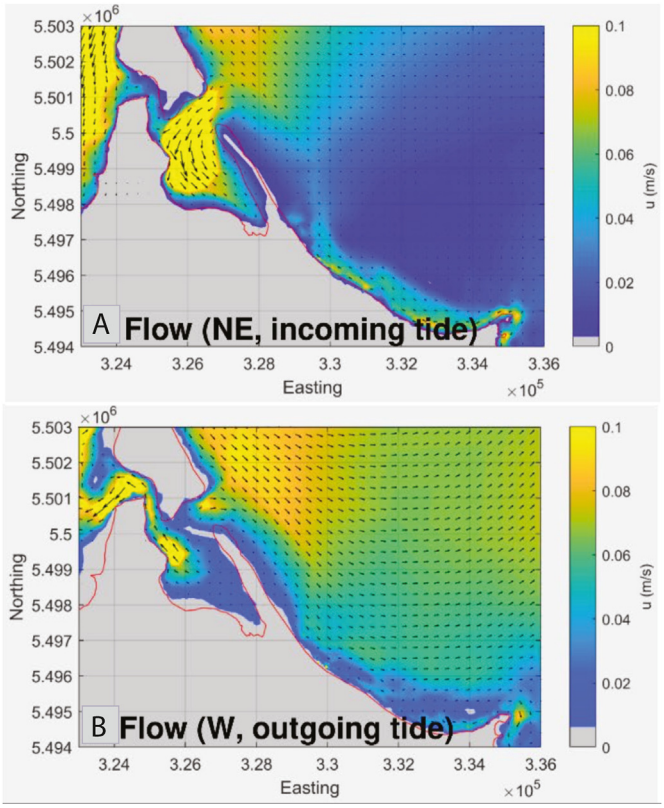

Fig. 5. Modelled modern hydrodynamic flow fields for: (a) Flood tide and NE waves; (b) Ebb tide and W waves, along the Ransonnet Bay coast of Robbins Island and Walker Island.

predominantly the gravelly sands on the NW West Tasmanian inner continental shelf and the shallower continental shelf within western Bass Strait (James et al., 2004) where semi-diurnal tidal currents form sandwaves extend from King Island towards Robbins Island (Malikides et al., 1988). Our modelling indicates that the dominant Holocene source of quartzose sand to form both the Ransonnet Coast and the Boullanger Bay coast has been supplied by sand transported from the western Tasmanian shelf into Boullanger Bay by westerly quadrant swell, and thence by net northward flood tidal current transport in Boullanger Bay. The tidal delta and channel morphology between Hunter Island and Robbins Island is indicative of the bidirectional tidal currents from the two tides that propagate into the region (Fig. 2). The ebb shield (Middle Bank) and ebb spits of the Walker Channel system are coupled to flood tidal delta sand lobe (Petrel Bank) to the north and east of Walker Island. The Petrel Bank is the primary source of sand, reworked by refracted westerly swell and northerly quadrant wind-sea waves to nourish and prograde the Ransonnet Bay coast of Robbins Island. Under easterly quadrant waves, sand from the Petrel Bank and Walker Channel ebb spits is transported longshore along the western Robbins Island coast to form a sequence of flying or recurved spits. Hence, these should be asynchronous with barwelding along the Ransonett Bay coast. The second pathway for sand transported from Boullanger Bay to Perkins Bay is by tidal current transport in Robbins Passage.

Analysis of aerial photographs and the bathymetry along the Ransonnet Bay Coast from Walker Island to the easternmost point of Robbins Island (Cape Elie) shows widespread basaltic reefs and minimal sand patches over the shoreface. This indicates that presently, there is insignificant sand transport from south-east to north-west along this coast. The Ransonnet Bay coast was split into three sediment compartments: (i) Walker Island to The Bluff; (ii) the Bluff to Guyot Point; and, (iii) Guyot Point to Cape Elie (Mortlock and Goodwin, 2018a,b). The bathymetry indicates that there is sand leakage from Petrel Bank out to 10 m water depth. With the predominantly low wave height-low wave period climate, we estimate that littoral exchange of sand between coastal compartments is restricted to shallower than the 5 m water depth.

4. MIS5e morphosedimentary record of sea level and wave climate

The morphosedimentary signature of the modern coast differs from the MIS5e Remarkable Banks embayment. The Holocene barrier is indicative of coastal evolution where horizontal accommodation space is limited with respect to modern sea level and shoreline aggradation has dominated the late Holocene. In contrast the MIS5e coastline formed a recessed shallow embayment with horizontal accommodation space for shoreline progradation and more sheltered to E wave energy than the modern shoreline. Taking note of those geomorphic differences we applied the modern beach berm/foredune and RR intertidal ridges and wave climate as 'a priori' for the modern analogue of the MIS5e Remarkable Banks.

4.1. Morphosedimentary sea-level indicator analogue

The east coast of Robbins Island experiences low wave energy and a meso tidal range ~3 m with a Relative Tidal Range (RTR) factor of 6. This results in a beach and surf zone morphology that is classified as tide-modified (after Short, 2006a; and b). The modern shoreface and beach morphology is shown in the LiDAR DEM (Fig. 6b). These show a high-tide reflective shoreline and a surf zone characterized by low amplitude shore-parallel sand bars that have a comparable wave length to the RB ridges. The shore-parallel sand bars accord with the classification by Short (2020), Masselink et al. (2006) and Scott et al. (2011) as the Ridge and Runnel (RR) type with 3–4 parallel sand-bar ridges exhibiting slip faces on their shoreward slope, are located in sub-tidal zone, with amplitude 100–150 m, and a nearshore slope of 1–2°. They are associated with fine to medium sand in low energy environments (H_b = 0.8–1 m) and short wave periods (T = 3–5 s) with macro-tides (4.2–6.5 m) (Scott et al., 2011). Masselink et al. (2006) found RR are subdued and migrate offshore during storms, then reform and aggrade in calmer conditions and slowly migrate shoreward. Our observations show that lower astronomical tidal cycles promote sand bar welding to the shoreline.

The modern beach berm and foredune planforms are aligned to the refracted W swell waves and the contemporaneous suite of RR type surf zone intertidal ridges are clockwise rotated and aligned to the incident NE waves. (see Fig. 6b). Hence, the sub tidal ridges, most likely form during NE storm wave periods and migrate offshore under strong infragravity frequency bed return flow and migrate shorewards under wave asymmetry during the longer period W swell. Intertidal sand-bar welding to the shoreline occurs when the bar sequence has migrated shorewards and is replaced offshore by a new ridge-runnel pair at the seaward limit of the surfzone. This sand-bar welding process is applied as the modern analogue for Remarkable Banks progradational ridge/swale sequence.

The indicative meaning (IM) for the paleo RSL is the indicative water depth of the feature. The IM is determined by two values: the indicative range (IR) (incorporating morphosedimentary and wave climate uncertainties) and the reference water level (RWL) or the mid-point of the IR (Van De Plassche, 1986; Shennan, 2015, expanded by Lorscheid and Rovere, 2019). In the Remarkable Banks case, the IM is the top of the welded inter-tidal bar sequence that defines the sea-level index point at −0.25 ± 0.45 m below MSL. The lower limit corresponds to the Mean Low Water Neap tidal datum. Where a sequence of 2 bars weld, the outer bar lies at −1.2 m ± (0.4 m) below MSL that is within the range for MLWS (−1.05 m) to LAT (−1.35). The IM for the beach face is +0.35 ± (0.15) m above MSL. Hence the IR elevation range of aqueous deposition including bar welding and runup is +0.35 to −1.2 m above MSL. In low wave energy settings such as Ransonnet Bay (Hs = 0.5 m), episodic bar welding occurs during lower astronomical and/or barometric/dynamic height tidal anomalies. Cross-bedded aeolian sands can be deposited as an incipient foredune cap between 0.5 and 1 m thick over the berm or welded bar surface.

4.2. Background on Holocene barrier record of sea level and wave climate change

The Holocene evolution provides an insight into the response of the Remarkable Banks paleoshoreline to RSL and directional wave climate changes. The Holocene outer Ransonnet Bay coastal barrier onlaps the RB, implying a Late Quaternary age for the latter (confirmed by OSL ages). The Ransonnet Bay coastal evolution is interpreted with respect to the modern coastal processes and the LiDAR DEMs shown in Fig. 6a and b. The Holocene barrier (HB) has filled the remaining horizontal accommodation space in the Ransonnet embayment post MIS5 to form Seven Mile Beach and Rockery Beach between Guyton Point on Robbins Island and Cathedral Rocks on Walker Island. Onlapping early-mid Holocene transgressive sands (overwash lobes) extend landwards between +2 and 3 m a MSL at the base of the barrier, and are capped by aeolian ridges 3–4 m high in places. The inundation of the seaward edge of the RB indicates an upper limit on Holocene RSL rise for the high tide plane to +2.5 m above modern high tide plane.

Four prominent shore parallel relic foredune ridges overlie the transgressive deposits along the Seven Mile Beach section and their alignment continues along the Rockery Beach barrier on Walker Island and form a continuous suite of planforms separated by Mosquito Sound and Channel. The inner margin of the HB is underlain in the south-east by boulder beach ridges that extend north-west from The Bluff. The buried boulder beach crest are ~0.5 m below the overlying sandy swales. At RI HBN02/17, shell deposits containing small bivalves (*Donax* and *Paphies* sp.) within the beach pebble units at 50 cm below the surface also contained molluscs and oysters, yielding an infinite radiocarbon age of 36.575–35.690 cal ka BP (Beta 483,637). Hence, we infer an MIS5 age for the inner buried boulder beaches. The mid to late Holocene relic foredune ridges have crests at 11–13.5 m and swale heights of 8–9 m above MSL, whilst the modern foredune ridge at the outer edge of the HB has a crest height of 7–8 m a MSL and a swale height of 5 m (Fig. 7 cross section). The fall in foredune swale elevation across the barrier indicates a RSL fall during the late Holocene (post the deposition of Ridge 2) of ~3 m. This is equivalent to the height differential of ~+3 m (+3.2–3.4 m corrected to +3.8 to +4.0 m above MSL) above modern for the mid Holocene-age Walker Island flood tidal morphology. OSL samples WAL02/19, WAL03/19 yielded ages of 5.5 ± 0.4 ka BP and 4.3 ± 0.4 ka BP respectively, whilst a 20–50 cm thick shell bed containing *Pupinella angazi* and various molluscan fauna collected at 50 cm depth yielded infinite radiocarbon ages of 40.671–39.304 cal ka BP (WAL02a/19, Beta − 529,808) and 40.671–39.304 cal ka BP (WAL03a/19, Beta − 529,808). This indicates that the Holocene tidal channel migration was eroding MIS5 subtidal sediments.

The onset of more continuous strandplain progradation commenced post 3 kyr BP and the planform geometry indicates a more energetic, possibly bimodal wave climate with a NE nearshore MWD of ~57° consistent with wave propagation from the NE in eastern Bass Strait. The most landward Ridge HBN2 (RI HBN02/17) yielded an OSL age of 2.8 ± 0.3 ka BP CAM (2.1 ± 0.6 ka BP and 4.7 ± 1.6 ka BP FMM), and Ridge HBN3 (RI HBN03/17) yielded an OSL age of 1.8 ± 0.2 ka BP. Post the deposition of HBN2, the planform geometry defines a clockwise rotation towards a more ENE MWD of 60° with the onset of recurved spit progradation into Mosquito Inlet. This is the modelled case for NE MWD combined with a dominant Tide 1 (westward propagating flood) (see Fig. 5a for the modelled flow field).

4.3. MIS5e Remarkable Banks morphosedimentary record

The evolution of Robbins Island and in detail, Remarkable Banks (RB) is shown in Fig. 7. The RB strandplain comprises ~140 low-amplitude sand ridges (~1 m amplitude and ~50 m wavelength) that are in excellent preservation with little to no aeolian reworking, except on the eastern Margin along the Robbins Passage coast. Here, a linear transgressive dune abuts and overlies the eastern edge of the RB paleoshoreline ridges. A water bore drilled on the transgressive dune ridge revealed that for 20 m below the sand ridges is a shell bioherm (beyond Radiocarbon dating limits and presumably of Quaternary age).

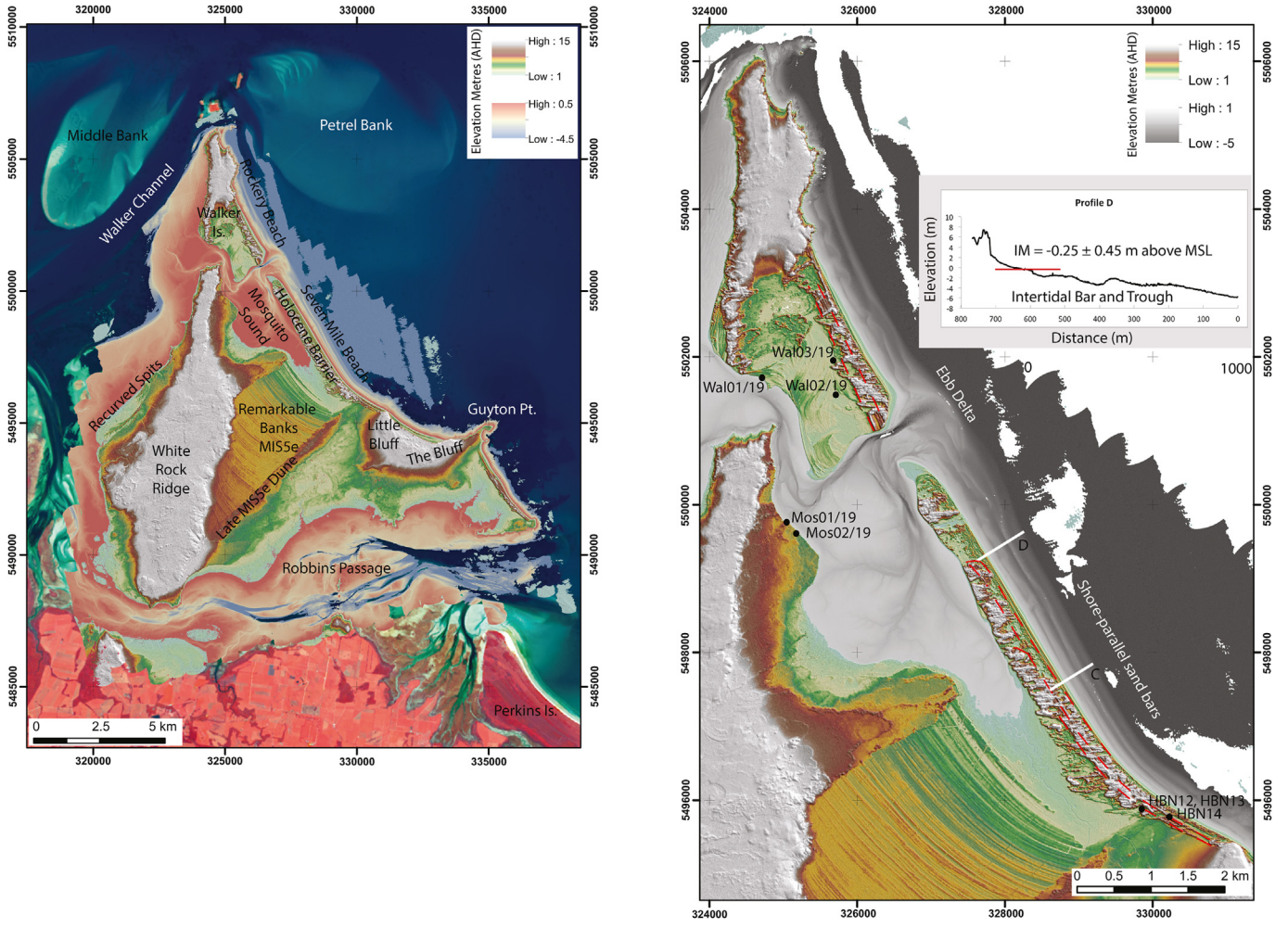

Fig. 6. Robbins Island Topo-Bathymetry LiDAR Digital Elevation Models (DEM): (a) Robbins Island showing key features including Remarkable Banks; and (b) Nearshore and intertidal Ransonnet Bay coast, Walker Island and the Holocene barrier, including the OSL sampling locations. The Holocene paleoshoreline planform sequence is shown in red dashed lines. A representative nearshore profile is also shown illustrating the intertidal bar and trough morphology. Also shown is the Indicative Meaning of the top of the welded bar at the shoreline. This is the SL analogue for the MIS5e interpretation.

The morphological fidelity of the RB ridges has permitted the investigation of their depositional environment, relationship to former sea-level, age of deposition, the progradation rate of the strandplain, and the evolution of the nearshore wave climate. A lack of subaerial reworking of the strandplain indicates a low onshore wind energy regime during deposition or lack of persistent storm wave erosion and sheltering from mid-latitude westerlies during the last glacial cycle.

The RB ridge caps comprised of: Unit 1 ~1 m of cream fine sand (2.5yr 12/9.5) with trough cross bedding; overlying Unit 2, a black brown sandy loam layer (7.5yr 2.5/1) below 1.5 m depth with seaward dipping (2°) laminations; and overlying Unit 3, a coffee red-brown sand (10yr 8/3) showing fine seaward dipping to planar laminations and trough infill, becoming weakly indurated at 3 m depth. The ridge swales contain ~0.2 m of Unit 1 cream fine sand over the Unit 2 black brown sandy loam and Unit 3. The water table lies within Unit 3. Below the upper unit of aeolian ridge cap, the Unit 2 is interpreted as beach face, and the remaining stratigraphy from Unit 3 to depth is interpreted as sub-aqueous and typical of intertidal surf zone bar and trough deposition (see Fig. 8b).

A total of 20 single grain OSL ages were obtained from samples taken across the RB profile. These are listed in Table 1 and are shown on the Remarkable Banks DEM in Fig. 7. All quoted OSL ages are computed using a CAM except for Remb01 and Remb12 that show over-dispersion and contain a MIS5e and MIS7 age population. Pit 15 also returned some CAM ages that were older than 150kyr BP and we have interpreted these as being pre MIS5e, most probably MIS7.

Field moisture contents are in general high (20–30%) for the OSL samples taken below 1.5 m or below the swale height as the RB forms a swamp in winter with surface water lying in the swales. The deep pit samples were taken just above the water table. We were unable to retrieve OSL samples from the ridges or swales landwards of Remb04 due to swampy conditions and slumping in auger holes, except at the landward edge of the RB at Remb01.

4.4. Remarkable banks strandplain progradation and RSL record

Topographic profiles of the modern Seven Mile beach and intertidal zone (Fig. 6b) were compared to the stratigraphy in the deep pits and the GPR radargrams (figure for the section between Pit3 and Pit 15). A long-section of the outer third of RB topographic profile extending to the modern surf zone is shown in Fig. 8a together with a GPR radargram and OSL sample locations and ages, and interpreted stratigraphy in Fig. 9a. The GPR radargram and pit exposures contain laminated bar strata and trough infill typical of

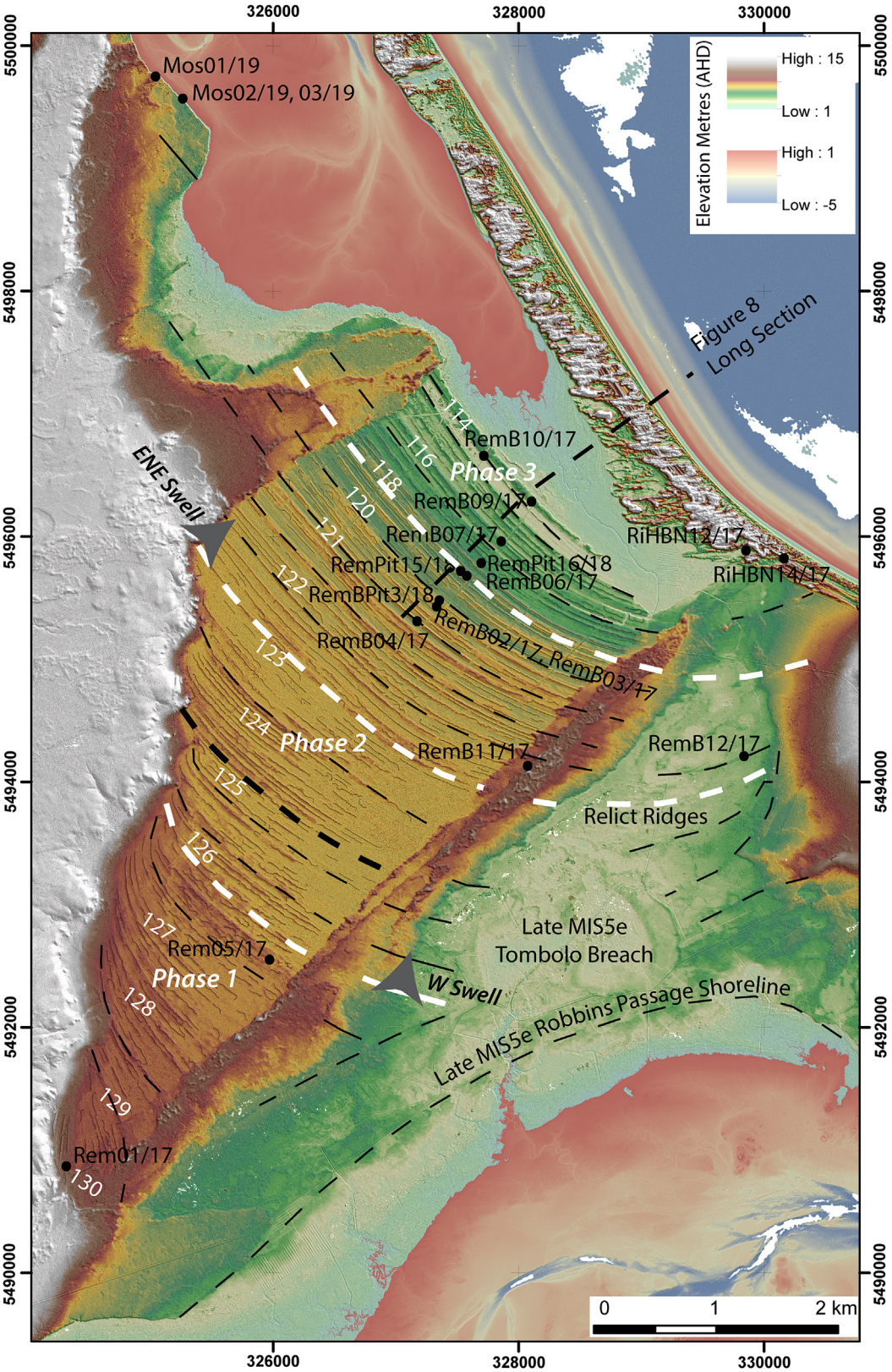

Fig. 7. Remarkable Banks DEM and coastal evolution phases during MIS5e. The location of OSL samples are shown together with the topographic profile shown in Fig. 8. The 3 phases of strandplain evolution are shown together with the paleoshoreline planforms, and nearshore wave direction orthogonals.

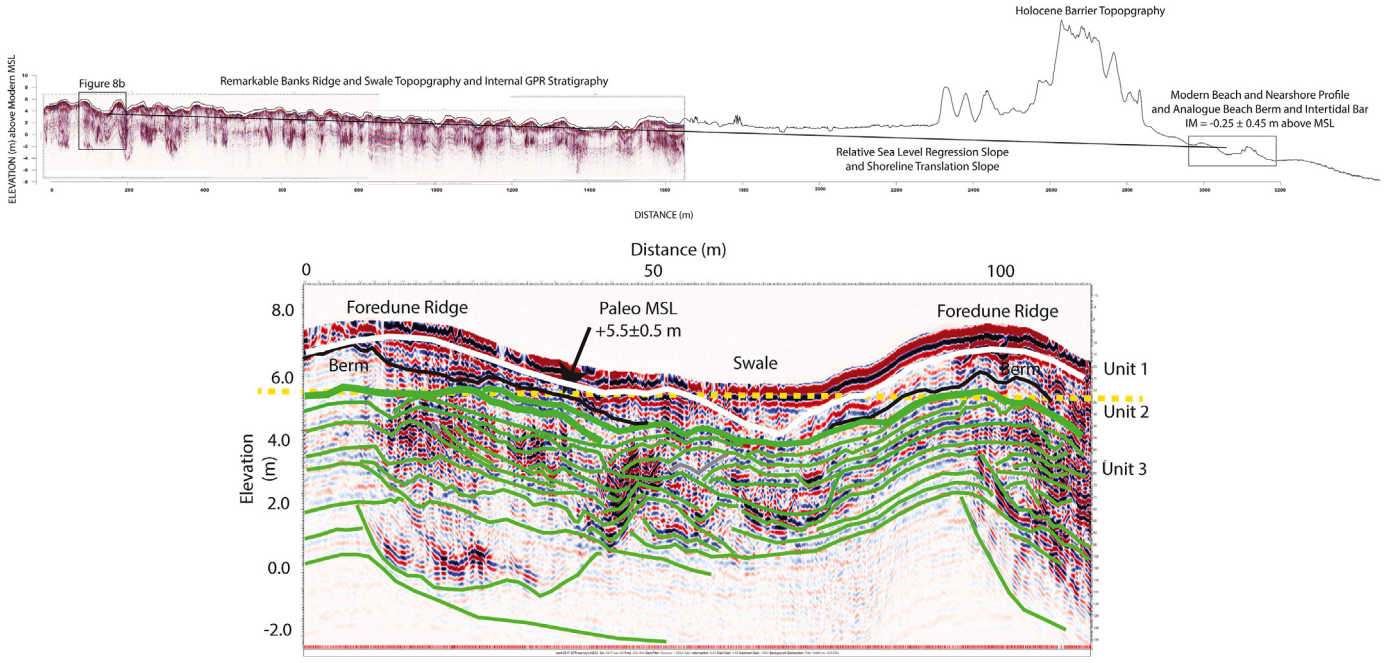

Fig. 8. (a) Topographic profile and GPR internal stratigraphy across outer Remarkable Banks, the Holocene Barrier and the modern beach and nearshore. The location of the profile is shown in Fig. 7. The slope through the swale elevations defines the slope for shoreline translation in response to RSL changes between the modern and MIS5e is shown. The slope passes through the modern nearshore bar and trough (the analogue RSL indicator morphology, as outlined by the box). Fig. 8 (b) shows the interpreted GPR radargram for a section of the RB containing two prominent ridges with a wavelength of ~90 m that matches the modern intertidal bar separation. The radargram shows the three units described in the text. The solid white line separates the Aeolian unit 1 from the beach face unit 2 with laminated seaward dipping strata. The solid uppermost green line denotes the top of the welded bar and the RSL indicator with the intertidal bar unit below. The intertidal bar unit comprises section sof trough cross bedding typical of bar crest deposits. The dashed yellow line delineates the paleo MSL in the mid MIS5e section at +5.5 ± 0.5 m above modern MSL.

the modern bar ridge and runnel morphology deeper than 2 m below the RB ridge surface (see enlarged GPR radargram in Fig. 8b. Hence, we interpret the core of the RB ridges to be welded nearshore intertidal bars from an ancestral surf zone type comparable to the tide-modified modern ridge and runnel morphology (described in section 4.1 above). The 0.2% topographic slope of RB (5 m in 3050 m) passing through the swales of the outer third of the RB intersects the modern surf zone runnels. This is taken as the shoreline translation profile as defined by the theory in Cowell et al. (2003). The presence of a defined shoreline translation profile is indicative that sea-level is the principle control of the shoreline position in the tide-modified energy regime and large variations in historical wave climate have not been a primary driver. Accordingly, we are confident that a continuum in the relative sea-level indicator across the RB supports the robust sea-level relationship for shoreline translation.

The preserved proxy sea-level indicator is the top of the welded bar with an IM of −0.25 ± 0.45 m below MSL (Fig. 6b). Across the RB, the top of the indicative MIS5e welded bar (Unit 3) is located at 1.5−2 m below the RB swale height over the entire 7 km RB. This locates the mid MIS5e MSL beneath Remb04 to Remb03 at +5.5 m ± 0.5 m above modern MSL. Based on this relationship we calculated the paleo MSL curve spanning stages 1, 2 and 3 that is shown in Fig. 9.

Additional data on the MIS5e RSL was obtained from Walker Island. The Holocene foredune ridges unconformably lie over a Late MIS5e tidal platform. We calculated the differential height between the modern ebb tidal delta surfaces and late MIS5e tidal platforms, that constrains the Walker Island late MIS5e RSL to be ~+3.8−4 m above modern MSL (based upon the +4.5 m elevation of the MIS5e Ebb Delta flat) (Fig. 6b).

The CAM ages show progressively younger ridge deposition seawards consistent with the strandplain depositional model. The surface slope of RB shows 3 distinct phases of deposition: Phase 1 RSL fall from 130 to 126 ka BP; Phase 2 stillstand from 126 to 121 ka BP; and, Phase 3 RSL fall from post 119 to 114 ka BP. Each of these stages of deposition occurred during different nearshore wave direction that is discussed below in section 5.3. To assess the rate of ridge deposition we assumed a linear progradation rate between chronological control in Phase 1 and 2. Phase 1 prograded at a rate of ~600 m per kyr with an individual ridge accreted every ~85 years. Phase 2 prograded at a rate of ~485 m per kyr with an individual ridge accreted every ~95 years. During Phase 2, progradation slowed to half the rate after 122 ka BP, and the ridge morphology shows episodic progradation with a more pronounced dune cap over the welded nearshore bar. The overall progradation rate between 122 and 120 is ~340 m per ka with an individual broad ridge accreted every ~200−250 years. Phase 3 prograded at a rate of 461 m per kyr with an individual ridge accreted every ~100 years. Hence, the MIS5e progradation occurred at the centennial scale.

The preserved RB strandplain is bordered to the NW and SE by longitudinal and parabolic dunes. The longitudinal dune onlapping the eastern edge of RB shows a 2-stage morphology (shown by the linear dune extent in the LiDAR DEM in Fig. 7). We interpret this dune as initially being deposited as a foredune along the tombolo linking White Rock Ridge with The Bluff forming the early to mid MIS5e Robbins Passage shoreline. An initial NW translation of the foredune occurred in conjunction with the breaching of the tombolo, forming a small lagoon behind. The morpho-stratigraphic relationship between the dune and the underlying Remarkable Banks ridges places the dune translation between 122 and 118 ka BP. The translational dune shows subsequent reworking. The dune has a deep core of red-brown indurated and mottled coffee rock that represents the original dune emplacement. Overlying this is a 2 m aeolian dune cap from which we obtained an OSL sample (Remb11/17) just above the coffee rock that was dated at 22 ± 2 ka

BP. This constrains the age of the longitudinal reworking of the dune tip (aligned to a prevailing SW wind direction 225–230°) during MIS2.

The Mosquito Sound dune scarp (5–8 m high) stratigraphy defined an aeolian origin overlying beach sediments forming a western extension of RB. We obtained OSL sand samples at +1.3 m and +4.5 m elevation where the stratigraphy contained fine heavy mineral laminations and trough cross bedding, overlying black coffee rock. The seaward dipping paleobeach sediments contained within the black coffee rock upper surface at + 3.5 m elevation are at the same height as those in the coffee rock outcrop at the outer edge of RB (Remb10) with an age of ~114 ka BP. OSL ages taken from the aeolian Unit 1, Mos01, Mos02 and Mos03 returned all MIS2 OSL ages of 22.8 ± 2, 25.4 ± 2.3, and 23.9 ± 2 ka BP respectively. The surface morphology shows parabolic dune tails and blowouts aligned to a 230–240° (SW) wind direction. The aeolian activity during MIS2 indicates strong SW wind energy being deflected around the White Rock Ridge.

5. Guyton Point boulder beach record

An extensive basalt boulder beach encircles Guyton Point (Fig. 6) with a series of concentric paleoshorelines and is connected to NE Robbins Island by a boulder tombolo. The boulder beach rises to +4.7 m to an emergent rock platform covered by an aeolian dune cap now covered by vegetation at +5 m. OSL samples were retrieved from the dune cap at +4.67 m (19.4 ± 2.1 ka BP, GuyP02/17) and +5 m (15.4 ± 0.5 and 16.7 ± 0.5 ka BP, GuyP01a and b/19). This indicates a pre Holocene and likely late MIS5e age for the +4.7 m emergent rock platform and uppermost boulder beach that is consistent with the MIS5e highstand of ~ +5.5 m determined at RB.

5.1. Robbins Island paleoshoreline planform geometry and wave climate

Examples of RB paleoshorelines from the 3 stages are shown in Fig. 9 and their matching wave refraction patterns from MIKE21 modelling are shown in the previous Fig. 5. The paleoshorelines deposited during Stage 1 of the RB have a parabolic planform spirally from a headland control point on White Rock Ridge, with the curvature flattening towards a salient apex in Robbins Passage. The nearshore Paleo MWD for Phase 1 is 330–10° (N) which aligns with refracted W swell. This is comparable to the Late Holocene westerly MWD. The Phase 2 paleoshorelines have a reversed planform geometry to Stage 1 and have a best fit paleo-MWD of 47° (NE) that align with the wind sea and swell windows from NE Bass Strait. This is comparable to the mid Holocene MWD from ~6 to 2 ka BP. From 120–118 ka BP, Phase 3 paleoshorelines rotate clockwise to a paleo MWD of ENE MWD (60°) (around Remb07 location) that aligns with the swell window from the Central Tasman Sea and eastern Bass Strait. This late MIS5e wave climate may have been bimodal W swell and E-ENE swell comparable to the late Holocene (post 2 ka BP). By 116–114 ka BP the MWD rotates anticlockwise to the W with a N Paleo-MWD similar to the late Holocene MWD.

Paleo MWD data was also obtained from boulder beach paleoshorelines at the NE tip of Guyton Point. These preserve a nearshore paleo MWD of 65–70° This MWD is aligned with the energetic swell window from the Central Tasman Sea that is capable of producing significant swash and runup to shape the cobble-boulder sized ridges. The ridges along the Guyton Point north coast and the tombolo have been breached up to +3–4 m elevation and reworked, with boulder lines running down drift of 65–70° MWD. The interpreted wave climate and elevated RSL accord with paleoshoreline formation post 119 kyr BP. It is possible that subsequent mid-Holocene reworking of the late MIS5e boulder beach has occurred under a +2.5–3 m highstand, together with ENE swell runup.

5.2. Robbins Island evolution model for MIS5e

The overall boundary conditions for the late Quaternary evolution of Robbins Island are a tide-modified environment with bimodal wave energy and strong bidirectional tidal currents, and an ongoing sand supply from the shallow continental shelf. The bedrock anchoring points for Quaternary sedimentation are the quartzite White Rock Ridge in the SW and the basalt bedrock hills (The Bluff) and offshore reefs in the NE. The water borehole logs revealed that for at least 20 m below RB the sediments comprise a molluscan shell bioherm that is typical of the subtidal environment

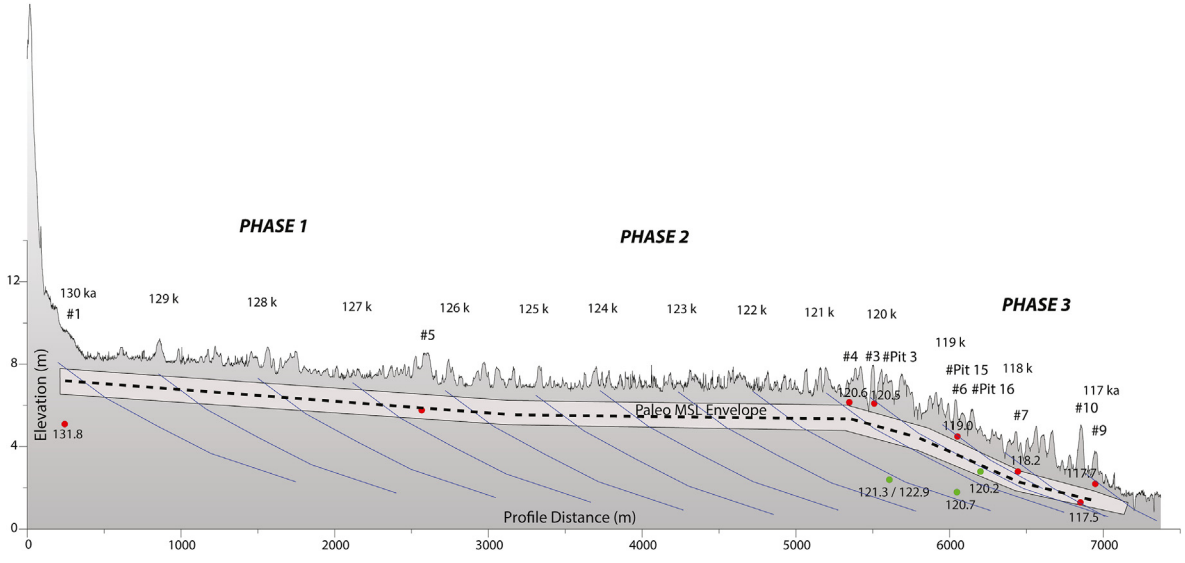

Fig. 9. Topographic cross section and interpreted sequence of paleo shoreline stratigraphy of Remarkable Banks, together with the sub-surface location of OSL samples and resulting ages. The interpreted MIS5e RSL envelope is also shown.

of the region. Inland of Robbins Island from Woolnorth to Stanley, the morphosedimentary evidence reflects an emergent distributary tidal system with modern analogues such as the Duck Bay, Robbins Passage and Boulanger Bay.

Previous studies have proposed late Quaternary neotectonism along the mainland Tasmanian coast (Murray-Wallace and Goede, 1995). We found no evidence for neotectonism between MIS7 and MIS5e or since, on Robbins Island. The RB strandplain onlaps a potential MIS7 age shoreface and estuarine surface as evidenced by the MIS7 age OSL population of unbleached sand grains mixed with MIS5e age sand near the margin of bedrock outcrops at White Rock Ridge and the Bluff. The inner strandplain elevation range of paleoshorelines on RB matches those modelled by GIA using late Quaternary ice models. In addition, the early to mid Holocene onlap shows that RSL at that time was equivalent to that during the late MIS5e (~114 ka BP) consistent with global sea level models. On NW Robbins Island, quartzite boulder and cobble raised beaches and a paleo tombolo outcrop in the 15–24 m. At the NW tip of Walker Island, a similar raised beach and shoreline outcrops at 20–21 m elevation. Banks (1989) reported sea caves and tunnels at 15–20 m on Albatross Island, north-west of Hunter Island and Robbins Island. These raised beaches and marine features lie stratigraphically at a pre MIS7 possibly Pliocene age. Their elevation range conform to other upper level ~20 m shorelines through northern Tasmania (Bowden and Colhoun, 1984, van de Geer, 1981) and the Bass Strait Islands (Sutherland and Kershaw, 1971), including a low sand plain extending across King Island that is underlain by marine shelly sand and mud sediments with an upper surface elevation of ~15–30 m, and equivalent paleoshorelines on Hunter Island.

The earliest MIS5e sedimentation from 130–127 ka BP was the deposition of spit then salient morphology extending from the southern tip of White Rock Ridge, and a second spit and salient formed SW of the Bluff, both oriented to refracted to bimodal W and E swell. The initial sequence of RB ridges prograded over the salient infilling the embayment to the north-east together with an aggrading foredune ridge bordering Robbins Passage (RPF). We interpret this progradation being coeval with RSL regression defined by the monotonic falling seaward slope of the RB ridges. The morphometrics indicate rapid progradation during the RSL fall and subsequent stillstand until 121 ka BP. This is expected where the shoreface slope is flat, combined with a net onshore sand transport from the lower shoreface, and a net sand transport to the Petrel Bank by wave and flood tidal currents from the NW Tasmanian shelf through Walker Channel.

At 126 ka BP, the RB salient rotated in response to a refracted wave pattern around the Bluff and to the south through Robbins Passage, due to a dominance of NE MWD. The paleoshoreline planforms indicate that the NE wave climate (53°) prevailed from ~126 to ~118 ka BP and resulted in ~65 low amplitude ridges comprising of welded intertidal bars under a low energy wave climate. The flat surface of the RB strandplain is indicative of an RSL stillstand during this period. The amplitude of ridges during the Phase 2 stillstand was low with minimal aeolian foredune accretion over the welded nearshore surf-zone bars. The low-lying morphology between the 2 salients indicates that an ebb tidal channel was draining Robbins Passage between RB and the Bluff.

Shoreline progradation was more episodic between 120 and 118 ka. This indicates coastal reorganization at this time involving either a declining sand supply or an increase in wave energy and storm erosion, or adjustment to falling RSL at the end of the stillstand. Since, the Remarkable Banks coast is reliant upon flood tidal current sand transport to feed the nearshore, any increase in NE wave energy would change the processes to be more wave dominated than tide dominated (see wave climate discussion in section 3.4).

The period of coastal reorganization is also defined by the breaching of the Robbins Passage tombolo, forcing the erosion and anticlockwise retreat of the Robbins Passage foredune and its translation west across the edge of the RB. The NW direction of the foredune translation defines a clockwise shift in wave climate to ENE MWD between 60 and 70°. Based on modern observations of the propagation of storm or long period swell waves from the Central Tasman Sea through the swell window between 55 and 70° in eastern Bass Strait, the Robbins Passage coast was potentially exposed to moderate wave energy. Such an increase in wave energy on a tide-modified coastline would result in overtopping and inundation such as that interpreted along the eastern Robbins Island coast. Modern storms in the Central Tasman Sea – eastern Bass Strait region such as the December 1998 and June 2016 produced an analogue for moderate wave energy events during 120–118 ka BP. These storms result in elevated water levels in Bass Strait from the barometric effect and wind and wave setup.

Renewed persistent strandplain progradation occurred from 118 to 114 ka BP, with the RB slope consistent with RSL regression from late MIS5e to 5 d. The increased amplitude of RB ridges between 120 and 114 ka BP indicates an a shift towards aggradation with RSL limiting accommodation space, or an increase in wave and wind energy, and/or sand supply rates. Between 118 and 117 ka BP the RB progradation resulted in a new Robbins Passage tombolo shoreline enclosing a shallow lagoonal basin whose remnant is visible in the DEM. The RSL at the time of closure of the lagoon was ~+3.4–3.6 m above modern MSL. The RSL fall and progradation of RB ridges NW towards Walker Island initiated erosion of the ridges now forming Mosquito Sound, by forcing tidal channel meandering.

5.3. Implications of MIS5e wave climate and coastal evolution for refining MIS5e RSL

The RSL across the RB relies upon the IM from the modern analogue and associated coastal processes and wave climate. Wave runup elevations, and intertidal bar and beach ridge amplitudes are directly forced by the directional wave power (Short, 1999). The reconstruction of MIS5e directional wave climate variability provides an opportunity to assess the robustness of the modern IM and its suitability to MIS5e. This is an application of the proxy-system modelling approach to centennial scale paleoclimatology that is best practice in high-resolution paleoclimate studies (Evans et al., 2013; Rovere et al., 2016). Directional wave climate variability is an important variable for RSL reconstruction since it controls modal and storm wave run up, beach face extent and storm erosion. Modern wave run up was empirically calculated in Mortlock and Goodwin (2018a,b) from modelled offshore wave parameters and cross-shore bathymetric transects, using the equation of Stockdon et al. (2006). This estimated that modern storm wave runup to be less than +0.95 m for 98% of the time (Hs = 5 m). Modal wave runup for Hs = 0.5 m was estimated to be less than 0.2 m.

The embayed setting of the MIS5e RB shorelines drives an increased wave refraction/diffraction and an attenuation of deep-water wave energy from the W and NE. Accordingly, during early MIS5e (Phase 1 wave type) the modern refracted w swell Hs would be less than 0.5 m. Similarly, the mid MIS5e (Phase 2 wave type, the modern NE wind sea Hs is estimated to be less than 0.5 m from the hydrodynamic modelling. The late MIS5e (phase 3 wave type) would have produced equivalent wave energy to that during the late Holocene and modern analogue. Therefore, the uncertainty in the upper bounds of early to mid MIS5e (129–121 ka BP) RSL is reduced due to negligible wave runup, leaving RSL variability as the primary driver of shoreline elevation. The revised IM for the RSL indicator based on sub-aqueous deposition including bar welding and runup is −0.25 to −1.2 m above MSL. The equivalent revision in

the MIS5e RSL during the stillstand is +5.75 ± 0.5 m.

6. The MIS5e sea-level index record for the Bass Strait region

6.1. Remarkable Banks observed and GIA modelled RSL records

The RB paleo MSL record over the duration of MIS5e has the potential to be an index site for SE Australia. In this section we compare the RB MSL record to the GIA modelled RSL and other Bass Strait RSL records to examine the accordance and discordance between sites. The boundary conditions for the GIA modelling are the same as those used for RB. The 7 km long RB topographic profile corrected to paleo MSL is applied as proxy MSL for MIS5e (Fig. 9). This attribution to paleo regional MSL is further strengthened by the equivalent mainland NW Tasmanian coastal plain surface slope profiles near Smithton (determined from the LiDAR DEM).

The modelled GIA curves for Robbins Island and the other Bass Strait Sites are shown in Fig. 10. An envelope of RSL curves is presented with the bold curve produced by our best-fitting mantle viscosity and lithospheric thickness values. These curves predict a monotonic fall in RSL throughout the MIS5e, as is expected for far-field locations from the former ice sheet centres. Instead, the observed Robbins Island RSL replicates the RSL fall predicted for Phase 1 and 3, but diverges with a stillstand during Phase 2. We attribute this departure to a persistent RSL rise from polar ice sheet meltwater contributions of at least ~2 m of sea-level equivalent during Phase 2. The Phase 2 stillstand is an ubiquitous feature of SE Australian MIS5e strandplains that in our view has previously been misinterpreted as evidence for an absent or subdued GIA response in the region. We use the observed Robbins Island RSL record as the reference record of 'real world' sea level during MIS5e that includes the composite GIA response together with the RSL rise from meltwater contributions.

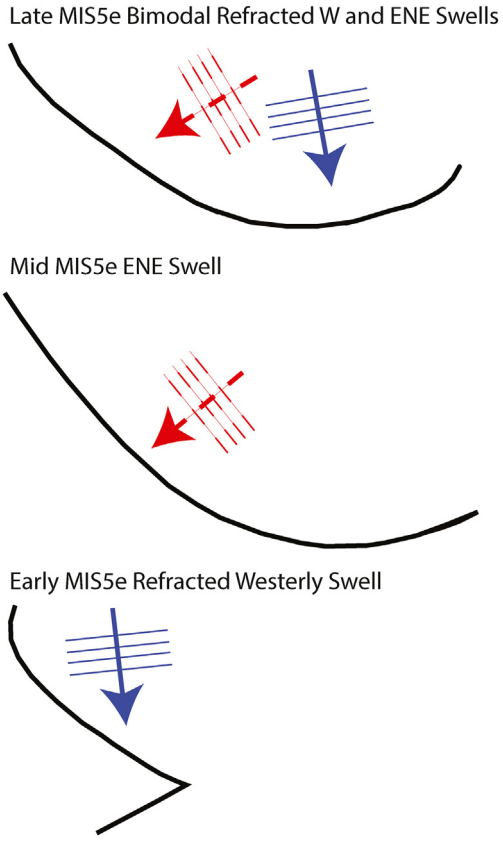

Fig. 10. Sequence of Remarkable Banks paleoshoreline planforms for the 3 phases of evolution, together with nearshore wave direction orthogonals.

6.2. Bass Strait observed and GIA modelled RSL records

Previous research on MIS5e coastal evolution and sea-level history has been conducted on: (i) Flinders Island (Sutherland and Kershaw, 1971; Murray-Wallace and Goede, 1995); (ii) King Island (Jennings, 1959; Murray-Wallace and Goede, 1995; D'Costa et al., 1993); Port Campbell (Jutson, 1927; Baker, 1943; Baker and Gill, 1957; Gill and Amin, 1975; Reeckman and Gill, 1981, and at nearby Warnambool by Carey et al., 2018); and Waratah Bay, Corner Inlet and East Gippsland (Jenkin, 1968; Bird, 1961, 1965; Bryant and Price, 1997; Gardner et al., 2008; Oliver et al., 2018). These sites encompassing Bass Strait contain no evidence for a widespread pattern of neotectonic uplift or 'hotspot reactivation' (Davies et al., 2015) during or since the MIS5e, with the exception of the South Gippsland, Victoria (north-east Bass Strait) region where Gardner et al. (2008) have conclusively demonstrated a sequence of tectonic uplift events since the Miocene along the Waratah Fault with last event at 70–80 ka BP. We investigated the evidence for MIS5e RSL history at these sites around Bass Strait to gain a regional understanding of sea-level variability and coastal response.

The coastal response at each location to RSL change during MIS5e is a function of the initial highstand and the subsequent rate of GIA decay. Note that the highstand and rate of decay of the GIA signal is dependent upon the inboard location of sites with distance from the continental shelf edge. Accordingly, we evaluate the field RSL indicators and GIA at each Bass Strait site to determine whether there is field evidence for coastal recession, stability or progradation. A caveat to this analysis is that the available data on MIS5e RSL around Bass Strait is disparate and from heterogeneous proxies, such that no complete RSL curve exists. Our additional results are based on fieldwork at Flinders Island, Port Campbell and Waratah Bay, and LiDAR DEM interpretation on King Island. We attempt to examine the RSL history with respect to the three phases at Robbins Island, and attribute the published ages and RSL indicators to each of those phases for comparative analysis. The MIS5e coast, planforms and sampling locations are shown in Fig. 11.

6.2.1. Flinders Island, eastern Bass Strait

Sutherland and Kershaw (1971) and Murray-Wallace and Goede, 1995 reported numerous localities where they interpret a +4.5 m former sea-level that they assign a Late Quaternary age. These include: (i) the East River lagoon inland of Cameron Inlet where a widespread coquina outcrop occurs within an inner barrier, (ii) the North east River (previously, Arthur River) coquina outcrop within in situ oyster bank and a 13 m high cliff exposed on the west bank of the tidal inlet opposite Beagle Spit; and, (iii) The North Patriarchs hard coquina, calcrete, and gravelly and gritty shelly sands and sandstone units. In addition, shore platforms cut in the Palana limestone.

We surveyed all sites in 2016, and found that the best preserved outcrop of coquina that also contained siliceous sands was the North East River site. Sutherland and Kershaw (1971) and Murray-Wallace and Goede, 1995 reported the stratigraphy at the site and we concluded that significant cliff recession had occurred since the previous surveys. The observed cliff bordering the estuary comprised of the following stratigraphy: An upper surface paleosol overlying cross-bedded fine dune sand to +5.4 m a MSL. Below this was the ~1.5 m coquina comprising the sequence of 0.5 m thick mollusc shell layer, over 5 cm thick calcrete, over a 0.5 m thick oyster bioherm, over a 0.5 m thick mollusk shell layer with *Laternulla* sp. In growth position. The Oyster bed is +3.5–4.5 m above

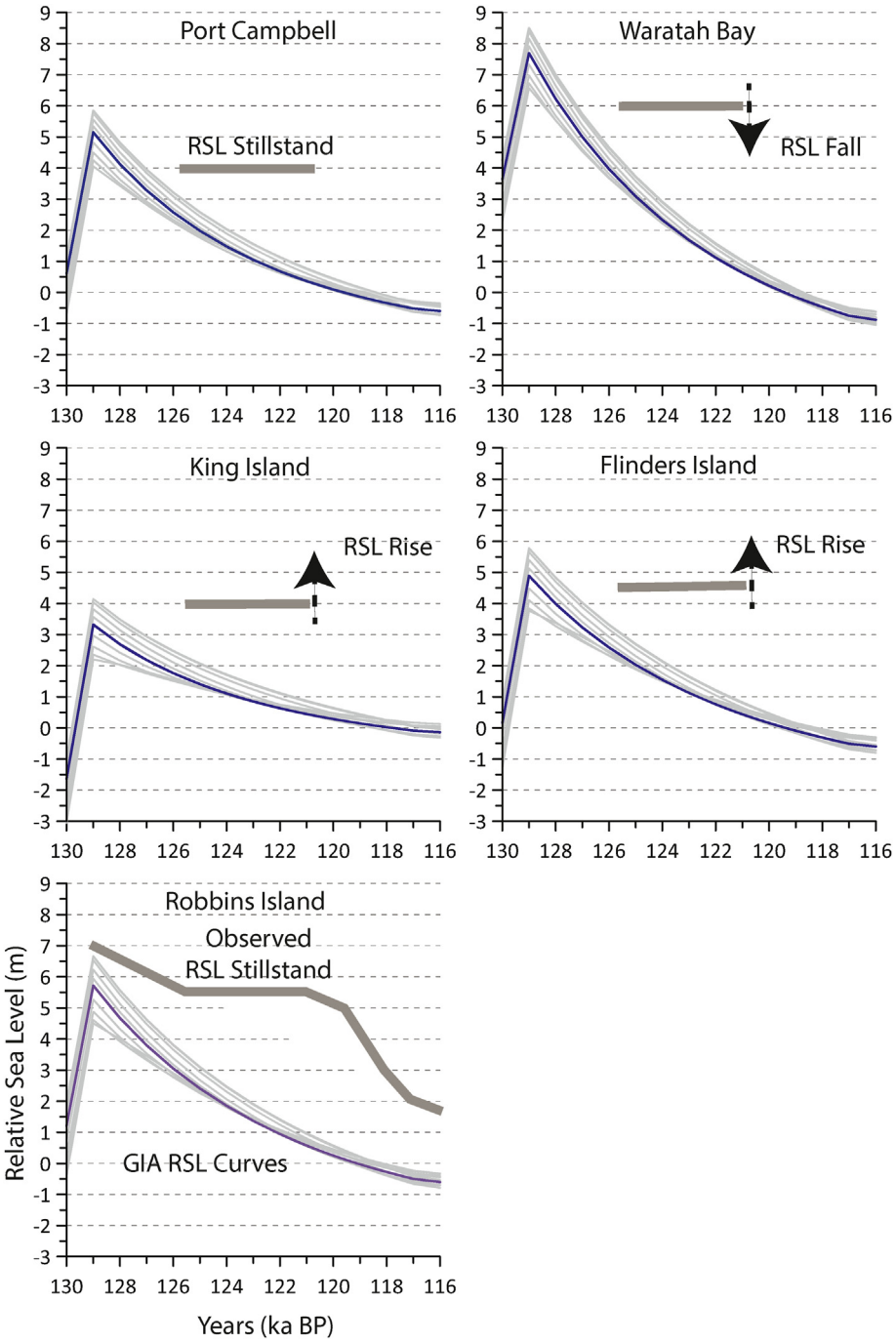

Fig. 11. Robbins Island and Bass Strait modelled GIA RSL curves together with observations of RSL indicators. These indicators are assigned a mid MIS5e age based on the available ages and their stratigraphic position. Using the Robbins RSL data, we postulate that at the other Bass Strait sites their RSL history should reflect the combination of GIA and meltwater contributions. Hence, at each site an arrow shows whether we interpret an RSL rise (lowest GIA highstand sites) or an RSL fall (highest GIA highstands) during the mid MIS5e period. This figure highlights that the observed regional RSL history will be different according to the initial highstand elevation produced by GIA (largely a function of distance to the continental shelf break).

modern equivalent and the *Laternulla* sp. shell bioherm is sub tidal to MLWN elevation. Beneath the coquina, are orange/yellow, fine-medium marine sands. Murray-Wallace and Goede, 1995 reported a MIS5e age for the *Laternulla* sp shell layer based on AAR and ESR dating methods. We sampled the upper dune sand unit (FI-NER-1F) and the lower marine sand unit (FI-NER-1B) immediately above and below the coquina for OSL dating. The OSL ages are 123 ± 10 ka and 127 ± 9 ka BP for the 2 units respectively (Table 3).

We interpret the marine sand below the coquina as flood tidal delta deposited at 127 ka BP, and that the upper aeolian dune sand constrains the age of the oyster bed to prior to 123 ka BP, when RSL was at least +3.5 to +4.5 m above modern. The overlying aeolian unit indicates coastline recession and barrier recession across the estuary during RSL rise post 123 ka BP. The observed RSL indicator is plotted on the modelled GIA curve in Fig. 11, that shows a modelled RSL at +4.5 m above modern at 125–124 ka BP. Using the Robbins RSL data, we postulate that at this site the meltwater contributions should have produced an RSL rise at 123–120 ka BP.

6.2.2. Waratah Bay, north-eastern Bass Strait

The northeastern Bass Strait coast includes Waratah Bay, Wilson's Promontory, Corner Inlet northwards to Lakes Entrance, and is situated within the Gippsland (intraplate) Basin. The MIS5e shore platform outcrops between 4 and 6 m at distance outside the axis of the Waratah Fault from Walkerville to east of Waratah Bay township. Onlapping these platforms is a calcarenite low foredune that has prograded over a longshore spit feature to the east, that defines a MIS5e paleoshoreline planform. Gardner et al. (2008) obtained OSL ages of between 122 and 132 ± 9 ka BP for the +4–6 m platforms at the western edge of the barrier/spit planform, and we interpret a post 122 ka BP age for the spit during coastal stability or slight RSL fall based upon the Robbins RSL data.

Seaward of the ~122 ka BP barrier are off-lapping barrier ridges with a seaward dipping surface slope indicates formation under the RSL fall, so we argue for a post 118 ka age based on the Robbins Island record. This is in good agreement with the GIA modelling of a fall in RSL from +6 to +5 m during 125–120 ka BP, and subsequent 2 m fall to 116 ka BP. This also conforms with a late MIS5e regressive strandplain and barrier at Sperm Whale Head, along the Gippsland coast north of Waratah Bay (Oliver et al., 2018).

6.2.3. Port Campbell coast, north-western Bass Strait

Emergent shore platforms at +4 m and up to +7.5 m, shallow water marine and beach sediments (Port Fairy Calcarenite), and aeolianite dunes (Dennington Sand) along the Otway Coast to the Port Fairy Coast were described by Jutson (1927), Baker (1943), Baker and Gill (1957), Gill and Amin (1975) and Reeckman and Gill (1981) as MIS5e age 110–125 ka BP from U-Series ages. Recent work at the Moyjil/Point Ritchie site near Warnambool dated shell with AAR and surrounding sands with OSL confirming a MIS5e age for shelly sand deposits overlying emergent shore platforms (Carey et al., 2018). The shelly sands contain molluscan fauna with *Anadara trapezia, Lunella undulata and Lunella torquate* as index species. These are warmer water fauna that are not found in the Holocene along this coast (Gill and Amin, 1975).

Shore platforms with notches at +3.5 to +4 m eroded into Miocene limestone with overlying shelly conglomerate layer grading to sand, outcrop in the modern coast between Warnambool and Port Campbell. Gill and Amin (1975) described three sites at Sandy Bay, Flat Rock, (east of Three Mile Bay or Dog Trap Bay) and at Two Mile Bay, west of Port Campbell. The latter site was first described by Jutson (1927). The conglomerate beach overlying the notch at +3.6 m with *Haliotis, Dicathais, Lunella undulata* shells that produced a U Series age of 107.9 ± 10.7 ka BP (Gill and Amin, 1975). A comparable conglomerate beach containing *Lunella torquata* overlying a basalt rock platform at +4 m near Port Fairy, yielded a U-series age of 125 ka BP (Gill and Banks, 1956). Taken together, these ages suggest a broad MIS5e age for the shore platforms.

We surveyed the Two Mile Bay, Port Campbell site. The site is partially sheltered to high-wave energy since Two Mile Reef (also known as Easter Reef) focuses long-period Southern Ocean swells to break about 1 km offshore. The site comprises of an emergent shore platform at +3.2 m above modern, overlain by a calcarenite unit defining a former beach surface that onlaps a stiff clay unit 2.1 m thick (up to 5.3 m a MSL). On the basis of the stratigraphic relationship with emergent rock platforms further west we interpret it as MIS5e. The upper third of this unit grades to sandy clay. The shore platform extends from the modern shoreline to terminate with a notch and visor in the Miocene cliffs. The latter have been preserved by a glacial-age low stand talus slope that has been eroded away during the Holocene along most of the coast. Modern rock platform IM relate to slightly above mean low water. This implies an RSL of +3.5–4 m above MSL for the emergent rock platform. The GIA response at Port Campbell is equivalent to that at Robbins Island. Hence, we postulate that the shore platform formed during the 126 to 121 ka BP stillstand.

6.2.4. King Island, western Bass Strait

Previous research has identified MIS5e deposits on King Island at Yellow Rock River (estuarine sediments at +3.7 m above modern MSL) and Egg Lagoon (+6 m) (Jennings, 1959; Murray-Wallace and Goede, 1995; D'Costa et al., 1993) and the Late Quaternary strandplain with raised shorelines forming the Lavinia Plain (Jennings, 1959). Multiple strandplain components indicate that it formed over at least 2–3 interglacials. The Lavinia Plain forms an inner barrier separated from the Holocene strandplain by a low-lying mature estuary, the Nook Swamp. The Lavinia remnant strandplain surface at +6–7.5 m and the seaward edge is defined by an erosion trimline. This potentially indicates that MIS5e RSL was below +6 m and is within the paleo RSL range of the Yellow Rock River estuarine sediments (+3.7 m above MSL is a minimum estimate). Whilst we have no age control for the Late Quaternary Lavinia Plain trimline we argue for a MIS5e age based on its morpho-stratigraphic location, and its planform geometry aligned to the reconstructed MIS5e wave direction. Using the Robbins RSL data, we postulate that at this site the meltwater contributions should have produced an RSL rise from +4 m at 123–120 ka BP.

7. MIS5e regional sea-level budget; influences of ocean wave climate, boundary currents and the subtropical ridge

7.1. MIS5e ocean wave climate

Recent studies such as Mortlock and Goodwin (2015), McSweeney (2020) and Liu et al. (2022) have investigated the wave climate of the SE Australian, Victorian and Bass Strait coasts. We investigate the MIS5e wave climate and its departure from the modern wave climate. Nearshore MIS5e MWD was reconstructed for western Bass Strait based on the Robbins Island paleoshoreline planform geometry and the tidal delta and spit geometry. This sequence defines a dominance of Southern Ocean W/SW swell entering Bass Strait during the early MIS5e (Phase 1), then a low energy NE-E wave climate during mid-late MIS5e (Phase 2), followed by a shift to back to a bimodal MWD distribution comprising of a dominant Southern Ocean W/SW swell mode and an E –NE swell mode (Phase 3) (Fig. 10). We explore the MIS5e paleoshoreline and spit morphologies in the available LiDAR and SRTM DEMs from sites around Bass Strait to build a regional wave climate history and implications for synoptic boundary conditions, such as the location of the STR. The DEMs, MIS5e shoreline planform geometry and nearshore MWD for each of the additional Bass Strait sites is shown in Fig. 12.

7.1.1. Flinders Island, eastern Bass Strait

Paleoshorelines were reconstructed along the north-east Flinders Island using the STRM DEM (Fig. 12). A defined transgressive barrier planform linking The Pattriarchs and NE River is conformal with the post 123 ka BP aeolian foredune cap at the NE River site. The subsequent formation of the middle barrier is consistent with the observed RSL fall from 118–116 ka BP at Robbins Island. The late Holocene shoreline planform is aligned to an E MWD and the post 123 ka BP planform is aligned to a SE MWD. The impact of MWD rotation between E and SE is well illustrated in the late Holocene foreland at Sellars Point, where wave refraction around Babel Island amplifies MWD changes.

7.1.2. King Island, western Bass Strait

The Lavinia Plain extends along the north–east and east coasts of King Island from Lavinia Beach and Point southwards along Nine

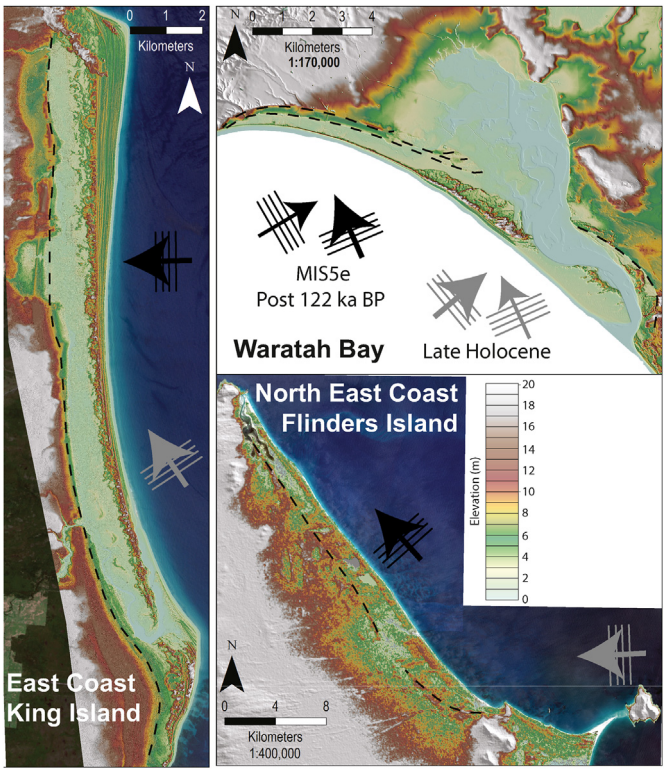

Fig. 12. Regional Bass Strait DEM's and Wave Climate changes during MIS5e for the East Coast of King Island, Waratah Bay, Victoria and north east coast of Flinders Island.

Mile Beach to Cowper Point. The coast is exposed to E quadrant wind-sea and swell from eastern Bass Strait and the Tasman Sea, but is in the shadow zone of the W-SW swell and prevailing W wind. Hence, the Lavinia coast receives strongly refracted W-SW swell around both the northern and southern ends of the island. Both Lavinia and Cowper Points form cuspate forelands and are sensitive to nearshore MWD shifts as a result of wave refraction and diffraction around the island.

The LiDAR DEM for the Lavinia Plain and east coast of King Island is shown in Fig. 12. We interpret that in general, the MIS5e shoreline trimmed and eroded into the older emergent strandplain, except for the Cowper Point foreland and the northern region between Lavinia Beach and Saltwater Creek where a strandplain and a high foredune was deposited at the seaward edge. The planform alignment of these regions is indicative of a prevailing E quadrant wave climate. The later MIS5e foreland at Cowper Point has a seaward surface dip similar to the regressive strandplains at the other sites after 118 ka BP. The Cowper Point foreland planform also shows a shift towards SW swell dominance (refracted to SE nearshore MWD) during the regression and the onset of renewed sand supply. These shoreline rotation during MIS5e have analogues during the Holocene changes. The Cowper Point foreland experienced a mid Holocene E MWD and then a period of refracted SW swell dominance during the Late Holocene, equivalent to that interpreted from Robbins Island to Perkins Bay.

7.1.3. Waratah Bay, northeast and Port Campbell, northwest Bass Strait

The paleo wave directions are determined with respect to modern wave buoy observations (vicwaves.com.au). The Holocene Waratah Bay shoreline is deeply embayed and forms a classic parabolic planform that is in static equilibrium to a nearshore MWD of 220–230° (period that is produced by the propagation of Southern Ocean SW swell through Bass Strait (peak swell direction and spreading of 228° ± 10° at nearby Inverloch wave buoy and 229° ± 20° at Wilsons Promontory wave buoy) (Fig. 12). The embayment also receives wave energy from a secondary SE mode with a MWD of 160° ± 12° (short - medium 5.6 s period mode from 155° ± 17° calculated from the Inverloch and Wilson's Promontory buoy records). The modern bimodal wave energy is dominated by the SW swell. In contrast the MIS5e age calcarenite dune/spit planform from Walkerville to Yanakie Dunes has reversed curvature, describing a parabolic planform that is aligned to W MWD and the dominant SE MWD (135–180° MWD) mode.

The modern Port Campbell coast is aligned to the S-SW MWD (peak swell direction and spreading for 213° ± 13° for period <10 s, and 205° ± 10° for period >10 s at Port Fairy wave buoy) whilst the MIS5e cliffed coast is rotated clockwise indicating a shift in MWD to the SW (~220°).

7.1.4. Ocean wave climate and large-scale climate change from back trajectory analysis

Since, ocean waves travel along Great Circles in deepwater, every coastal compartment can be assigned unique swell and wind-sea directional windows, that link the coastal archive with the wave generation source region or propagation path. Back trajectory analysis of the nearshore/shoreface paleo-wave direction can be conducted using the unique great circle paths emanating from the coastal location to identify the potential locus of wave generation. The back trajectory analysis can be conducted for the time-series of paleo-wave direction estimates to produce a time series of Weather Regimes (based on unique parametric wave data, see Mortlock and Goodwin, 2015 and Goodwin et al., 2016) from which an understanding of changes in atmospheric circulation can be inferred (Goodwin, 2023) .

The Robbins Island to Perkins Bay coast has back trajectory swell windows external to Bass Strait of 235–270° (Southern Ocean W and WSW) and 55–70° (Central Tasman Sea) wave climate types. Waratah Bay has narrow swell windows of 250–270° and 220–230° corresponding to Southern Ocean W and SW wave climate types, together with 135–180° for Eastern Bass Strait and 133–137° for South Tasman Sea wave climate types (Fig. 13). The east coast of Flinders Island is sheltered from the W and SW wave climates whilst it is exposed to a wide window 40–180° of NE to S wave climates stretching from the northern Tasman Sea to the Southern Ocean. The east coast of King Island is also sheltered from the W and SW wave climates, but is exposed to a very narrow window from the ENE 60–75° MWD, that corresponds to Central Tasman Sea and eastern Bass Strait wave climates.

When the array of Bass Strait nearshore MWD for MIS5e are traced back along the swell window angles they intersect to resolve a unique solution for the prevailing wave climate source region and hence, insight into atmospheric circulation. Bass Strait experienced during: (i) early MIS5e, a dominant W/SW Southern Ocean swell climate; (ii) mid to late MIS5e, a shift to ENE Central-Southern Tasman Sea swell and eastern Bass Strait wind sea and moderate period swell with an E-SE MWD; and (iii) late MIS5e, a shift to a bimodal wave climate comprising W/SW Southern Ocean swell climate, and ENE Central Tasman Sea swell and E-SE moderate period swell generated in eastern Bass Strait. The mid to late MIS5e MWD at each site is sub-parallel to that interpreted from the mid-Holocene planform geometry.

Based on modern wave observations and relationships with the STR latitude (Goodwin et al., 2016) and the storm track as defined by the Southern Annular Mode index (SAMi, see Marshall, 2003) the MIS5e wave climate indicate significant shifts in mid-latitude climate. The early to mid MIS5e wave climate shifts require the

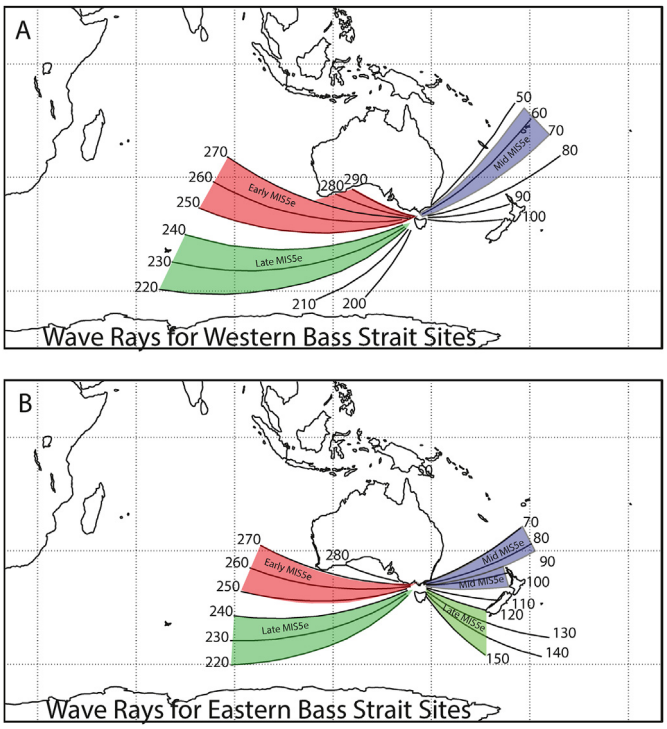

Fig. 13. Great circle ray envelope for ocean wave propagation to: (a) Robbins Island and western Bass Strait sites; and, (b) eastern Bass Strait sites. The wave rays are shown for early MIS5e (red), middle MIS5e (blue) and late MIS5e (green). The units for the rays are true bearing degrees. The ray envelopes define the possible locations of wave generating synoptic systems in the Southern Ocean and Tasman Sea that propagate into Bass Strait.

mean STR ridge latitude to have expanded polewards by at least ~5° S relative to modern between 126 and 119 ka BP. Modern seasonal observations show that a poleward shift in the STR and storm track (positive SAMi) results in an anticlockwise rotation of swell wave direction in Bass Strait (McSweeney, 2020; Liu et al., 2022). As a consequence, Bass Strait, SE Australia, northern and eastern Tasmania experienced a predominance of tradewind and anticyclone generated wave climate from ~126 to 119 ka BP. The anticlockwise rotation along the Flinders Island and Waratah Bay coasts is forced by the anticlockwise rotation of Southern Ocean swell in the shadow zone east of Tasmania, giving rise to a shift to more S and SE MWD (after McSweeney, 2020; Liu et al., 2022). Post 119 ka BP the mean STR migrated northwards to close to modern mean latitude to produce a clockwise-rotated wave climate similar to modern.

Overall, the anomalous paleo wave climate describes a very distinct atmospheric circulation, with a poleward shift in the STR and anticyclone intensification either over the southern Tasman Sea or E and NE of New Zealand that forces a dominant E quadrant windfield and wave generation in the Tasman Sea and in Bass Strait. The paleo MWD at each of the sites indicates periods of NE, E and SE wave climate in the Tasman Sea and Bass Strait associated with either a NE or SE tilt in the anticyclone axis.

Whilst, a detailed reconstruction of the MIS5e atmospheric circulation and weather regime anomalies are reconstructed in a separate paper (Goodwin et al.), a short summary is included below. The sequence of regional wave climate anomalies from Southern Ocean Westerlies to regional Bass Strait and Tasman Sea easterlies, then back to Southern Ocean Westerlies during MIS5e describes a multi-millennial scale shift in the storm track. The mid MIS5e shift to easterly wave climate is typical of conditions during modern anticyclone intensification when the atmospheric South Pacific split jet results in a strengthening of the subtropical and subpolar jets and a weakening of the mid-latitude jet. The pattern results in a strong blocking of the westerly circulation to 50°S in the Tasman Sea longitudes and deflection of the mid-latitude to a subpolar storm track with W MWD Southern Ocean swell propagating southwards away from SE Australia. This resulted in a low energy Tasman Sea wave climate (Goodwin et al., 2016, Goodwin, 2023). In addition, summer anticyclone intensification over the SE Australia and Southern Tasman Sea occurs during moderate to strong La Nina-like climate (see eg. February 2022).

A strengthened Austral winter South Pacific split jet during the mid to late MIS5e (~124–116 ka BP) is consistent with a split jet maximum during maximum winter precessional insolation at ~123–124 ka BP (after Lamy et al., 2019), possibly reinforced by the interhemispheric atmospheric teleconnection from a warm North Atlantic region (after Chiang et al., 2014). This resulted in the strong signal of anticyclonic intensification and 5° latitudinal shifts in the STR over the Tasman Sea and SE Australia together.

7.2. MIS5e boundary current and barometric effects on regional SL budget

Regional RSL history can be impacted by changes in dynamic heights due to boundary current shifts and/or changes in mean atmospheric pressure (inverse barometric effect). We attempted to conduct a paleo sea-level budget to address whether our interpreted RSL history contains climate-forced SL variability. Modern STR seasonal climatology, indicates that a sustained shift to a more summer-like pressure field and ~5° poleward STR shift (see Fig. 1b), would have lead to a relative fall in pressure of ~4 hPa and an inverted barometric pressure effect of + ~0.04 m on Bass Strait SL. Such a poleward STR shift would also reduce the potential for elevated RSL events in Bass Strait due to the reduction in the passage of cold fronts influencing the region.

An early to mid MIS5e strengthening and southward extension of the East Australian Current is indicated by the poleward range extension of hermatypic corals along the east coast of Australia to at least 33° S (Marshall and Thom, 1976; Pickett, 1981; Pickett et al., 1989, Goodwin, 2023), and a warming in Southern Ocean SST's south of Tasmania (Cortese et al., 2013; Chadwick et al., 2020). Modern observations have shown that over the past 70 years, the EAC has strengthened, extended polewards by ~300 km to Tasmania and the SST's in eastern Bass Strait and the east coast of Tasmania have warmed by 2–3° (Hill et al., 2011). This is in response to a strengthened (weakened) subpolar (mid latitude) jet and a spin-up of the South Pacific Gyre.

In addition the SL variability along the western Bass Strait region is influenced by the poleward flowing eastern Indian Ocean boundary current (Leeuwin Current) that flows anticlockwise along the Southern Australian shelf to become the Zeehan Current that terminates around Tasmania (Cresswell, 2000). The Leeuwin and Zeehan Current system is seasonal and causes seasonal SL near western Bass Strait to vary by 0.1 m. The Leeuwin Current was interpreted to be stronger and warmer along the SWWA shelf from the observed southwards range extension of corals during the early to mid MIS5e (McCulloch and Esat, 2000; McCulloch and Mortimer, 2008). Similarly molluscan and coral fauna typical of warmer than Holocene SST was reported in MIS5e barriers in the Great Australian Bight (Murray-Wallace et al., 2000, 2016; Pan et al., 2020) and along the Victorian west coast from Port Fairy to Port Campbell (Gill and Amin, 1975). This indicates a more persistent and warmer Zeehan Current along the western Bass Strait and shelf during early and mid MIS5e. A strengthened Zeehan Current causes upwelling off NW Tasmania and Robbins Island experiences a −1° SST for a +1° SST in the Zeehan Current, driving a +ve SL anomaly. Hence,

the combined influence of the EAC and LC/ZC on the interpreted RSL history is for an implied + ve SL contribution of ~0.2 m between 127 and 120 ka BP followed by a −ve SL contribution post 119 ka BP of a similar magnitude.

8. Conclusions

The Remarkable Banks, Robbins Island morpho-stratigraphic archive contains the most complete MIS5e RSL index-record in Australia. Our work on Robbins Island and Walker Island provides no evidence for late Quaternary neotectonism affecting the fidelity of the MIS5e RSL record. The unique marginal sea environment with low wave and wind energy, prevalent upper shoreface sand supply and a tide modified morphodynamic regime resulted in the deposition of high spatio-temporal fidelity in recording RSL. This enabled the analysis of observed RSL history to be compared to modelled RSL history due to GIA forcing over the full interglacial. The RB RSL record describes a multi-millennial stillstand from ~126 to ~121 ka BP at 5.75 ± 0.5 m above MSL instead of the theoretical exponential SL regression decay curve for GIA alone. Interestingly, previous researchers (Murray-Wallace et al., 2016; Pan et al., 2020) have also concluded from fragmentary RSL records in Australia for a RSL stillstand at +3.7 to 4.8 ± 1 m aMSL during MIS5e. In essence, all these RSL records are in agreement and the observed Southern Australian stillstand departure from GIA theory at all sites, points unambiguously to persistent polar meltwater contributions to sea level rise from 126 to ~121 ka BP. Hence, the observed stillstand represents a balance between where GIA-induced RSL fall rates and meltwater-induced RSL rise rates.

The GIA highstand and decay rate varies at sites around Bass Strait due to their different geographic locations inboard from the continental shelf break. Where there is a subdued GIA response, the RSL rise from meltwater resulted in an RSL transgression. Hence, the observed RSL stillstand at Robbins Island translates into a slight transgression at Port Campbell, King Island and Flinders Island, and an early slight transgression then regression at Waratah Bay. The geographic variability in the local RSL height for mid to late MIS5e around Bass Strait highlights the need for a regional approach to be taken in paleo SL investigations to address GIA processes and site specific highstand elevation and decay rates. Our SL budget approach and co-reconstructions of RSL and MWD provides a complimentary investigation of hydrodynamic forcing of shoreline behaviour.

The array of paleoshoreline planforms allowed the triangulation of MWD sources to develop a combined paleo wave climate history for Bass Strait. This together with the available paleontological and marine sedimentary evidence from SWWA to eastern Australia indicates Tropical Expansion of atmospheric − ocean circulation during MIS5e, The key atmospheric circulation anomaly that best fits the observed pattern of wave climate change and low wind climate during the mid to late MIS5e, is an anticyclone intensification over the Tasman Sea and SE Australia and Tasmania. The associated ~5° poleward shift in the STR and westerly storm track during mid-late MIS5e, is consistent with a strengthening of the Austral winter South-west Pacific subtropical jet, and an extreme shift towards a La Nina-like climate and positive SAM background state during Austral summer.

Author contributions

The overall project idea was prepared by IDG. Fieldwork was conducted by IDG and MOL. Digital elevation models were prepared by MOL, IDG and MR. Modern sea-level analogue, climate, sea-level and wave data analysis, and hydrodynamic modelling was conducted by TRM and IDG. The OSL geochronology was developed by RW (laboratory analysis) and IDG (data analysis). Ground penetration radar surveys were conducted by IDG and radargrams were prepared by IDG and MR. The GIA modelling was contributed by JXM. The interpretation of the coastal morpho-sedimentary data and the paleo-wave climate analysis was conducted by IDG. The manuscript was prepared and written by IDG with editorial contributions from TRM, JXM, and MOL. The figures were prepared by IDG, MOL, MR and TRM.

Funding sources

This work was funded by the Australian Research Council Discovery Project scheme (ARCDP16 16012561 Project) to CIs IDG (lead), MOL and JXM. The modern coastal process and hydrodynamic modelling work was in part funded by a consulting contract from GHD and UPC Renewables to IDG.

Declaration of competing interest

The authors declare that they have no known competing financial interests or personal relationships that could have appeared to influence the work reported in this paper.

Data availability

Data will be made available on request.

Acknowledgements

We thank John and Alex Hammond, Hammond Farms, Montague, Tasmania for their hospitality, local knowledge and logistical assistance in conducting field work on Robbins Island. We thank Dr Zac Larkin for field assistance, and Emeritus Professor Eric Colhoun for first introducing the site to IDG in the 1990's. We thank Dr Jorge Hacker, Airborne Research Australia for providing high resolution LiDAR coverage of the island under contract to the project. We thank A/Prof Kira Westaway for her supervision in the TRAPS-Macquarie OSL Laboratory and for discussions about the OSL dating results.

References

Aitken, M.J., 1998. An Introduction to Optical Dating. Oxford University Press, Oxford.
Baker, G., 1943. Features of a victorian limestone coastline. J. Geol. 51 (6), 359–386. Aug. - Sep., 1943.
Baker, G., Gill, E.D., 1957. Pleistocene emerged marine platform, Port Campbell, Victoria. Quaternaria 4, 1–14.
Banks, M.R., 1989. Notes on the geology and geomorphology of Albatross island. Rec. Queen Vic. Mus. 95.
Barlow, N.L.M., et al., 2018. Lack of evidence for a substantial sea-level fluctuation within the last interglacial. Nat. Geosci. 11 (9), 627–634.
Bird, E.C.F., 1961. The coastal barriers of East Gippsland, Australia. Geogr. J. 127, 460–468.
Bird, E.C.F., 1965. The evolution of sandy barrier formations on the East Gippsland coast. Proc. Roy. Soc. Vic. 79, 75–88.
Bowden, A.R., Colhoun, E.A., 1984. Quaternary emergent shorelines of Tasmania. In: Thom, B.G. (Ed.), Coastal Geomorphology in Australia. Academic Press, Sydney, pp. 313–342.
Brooke, B., et al., 2019. Relative sea-level records preserved in Holocene beach-ridge strandplains – an example from tropical northeastern Australia. Mar. Geol. 411, 107–118, 2019.
Bryant, E.A., Price, D., 1997. Late Pleistocene marine chronology of the Gippsland Lakes region, Australia. Phys. Geogr. 18, 318–334.
Carey, S.P., Sherwood, J.E., Kay, M., McNiven, J., Bowler, J.M., 2018. The Moyjil Site, South-West Victoria, Australia: Stratigraphic and Geomorphic Context, vol. 130. The Royal Society of Victoria, pp. 14–31. https://doi.org/10.1071/RS18004, 2018.
Chadwick, M., Allen, C.S., Sime, L.C., Hilenbrand, C.-D., et al., 2020. Analysing the timing of peak warming and minimum winter sea-ice extent in the Southern Ocean during MIS 5e. Quat. Sci. Rev. 229, 106134, 2020.
Chiang, J.C.H., Lee, S.-Y., Putnam, A.E., Wang, X., 2014. South Pacific Split Jet, ITCZ shifts, and atmospheric North–South linkages during abrupt climate changes of

the last glacial period. Earth Planet Sci. Lett. 406, 233–246, 2014.
Clark, P.U.F., et al., 2020. Oceanic forcing of penultimate deglacial and last interglacial sea-level rise. Nature 577, 660–664.
Cortese, G., et al., 2013. Southwest Pacific Ocean response to a warmer world: insights from Marine Isotope Stage 5e. Paleoceanography 28 (3), 585–598.
Costas, S., Ferreira, O., Plomaritis, T.A., Leorri, E., 2016. Coastal barrier stratigraphy for Holocene high-resolution sea-level reconstruction. Sci. Rep. 6, 38726. https://doi.org/10.1038/srep38726.
Cowell, P.J., Stive, M.J.F., Niedoroda, A.W., de Vriend, H.J., Swift, D.J.P., Kaminsky, G.M., Capobianco, M., 2003. The coastal-tract (part 1): a conceptual approach to aggregated modeling of low-order coastal change. J. Coast Res. 19, 812–827.
Cresswell, G.R., 2000. Currents of the continental shelf and upper slope of Tasmania, Pap. Proc. R. Soc. Tasmania 133, 21–30.
d'Costa, D.M., Grindrod, J., Ogden, R., 1993. Preliminary environmental reconstructions from late quaternary pollen and mollusc assemblages a t Egg lagoon, king island, Bass Strait. Aust. J. Ecol. 18, 351–366.
Davies, J.L., 1972. Geographical Variation in Coastal Development. Oliver and Boyd, Edinburgh, p. 204.
Davies, D.R., Rawlinson, N., Iaffaldano, G., Campbell, I.H., 2015. Lithospheric controls on magma composition along Earth's longest continental hotspot track. Nature 525, 511–514. https://doi.org/10.1038/nature14903.
Dendy, S., Austermann, J., Creveling, J.R., Mitrovica, J.X., 2017. Sensitivity of Last Interglacial sea level high stands to ice sheet configuration during Marine Isotope Stage 6. Quat. Sci. Rev. 171, 234–244.
DHI, 2016. MIKE21/3 Coupled Model FM User Guide, MIKE by DHI. Danish Hydraulics Institute, Denmark, p. 52.
Donaldson, P., Sharples, C., Anders, R., 2012. The Tidal Characteristics and Shallow-Marine Seagrass Sedimentology of Robbins Passage and Boullanger Bay, Far Northwest Tasmania. In: A Technical Report to Cradle Coast NRM by Blue Wren Group, vol. 88. School of Geography and Environmental Studies, University of Tasmania, 2012.
Drosdowsky, W., 2005. The latitude of the subtropical ridge over Eastern Australia: the L index revisited. Int. J. Climatol. 25 (10), 1291–1299. https://doi.org/10.1002/joc.1196.
Durrant, T., Greenslade, D., Hemer, M., Trenham, C., 2014. A Global Wave Hindcast Focussed on the Central and South Pacific. The Centre for Australian Weather and Climate Research: a partnership between CSIRO and the Bureau of Meteorology, p. 54. CAWCR Technical Report No. 070, April 2014.
Dutton, A., Lambeck, K., 2012. Ice volume and sea level during the Last Interglacial. Science 337, 216–219.
Dutton, A., Webster, J.M., Zwartz, D., Lambeck, K., Wohlfarth, B., 2015. Tropical tales of polar ice: evidence of Last Interglacial polar ice sheet retreat recorded by fossil reefs of the granitic Seychelles islands. Quat. Sci. Rev. 107, 182–196. https://doi.org/10.1016/j.quascirev.2014.10.025, 0277-3791.
Dutton, A., Villa, A., Chutcharavan, P.M., 2022. Compilation of Last Interglacial (Marine Isotope Stage 5e) sea level indicators in the Bahamas, Turks and Caicos, and the east coast of Florida, USA. Earth Syst. Sci. Data 14, 2385–2399. https://doi.org/10.5194/essd-14-2385-2022, 2022.
Evans, M.N., Tolwinski-Ward, S.E., Thompson, D.M., Anchukaitis, K.J., 2013. Applications of proxy system modeling in high resolution paleoclimatology. Quat. Sci. Rev. 76, 16–28.
Everard, L., Calver, C.R., Pemberton, J., Taheri, J., Dixon, G., 1997. Geology of the islands of southwestern Bass Strait. Tasmanian Geological Survey pp64. Record 1997/03.
Gardner, T., et al., 2008. Episodic intraplate deformation of stable continental margins: evidence from Late Neogene. Quat. Sci. Rev. https://doi.org/10.1016/j.quascirev.2008.10.004.
Gill, E.D., Amin, B.S., 1975. Interpretation of 7.5 and 4 metre Last Interglacial shore platforms in southeast Australia. Search 6, 394–396.
Gill, E.D., Banks, M.R., 1956. Cainozoic history of Mowbray Swamp and other areas of north-western Tasmania. Rec. Queen Vic. Mus. Launceston 6, 1–41.
Goodwin, I.D., 2023. Synoptic Paleoclimatology. Cambridge University Press in prep.
Goodwin, I.D., Browning, S., Mortlock, T.R., 2016. Tropical-Extratropical origin storm wave types and their influence on the East Australian Longshore Sand Transport System under a changing climate. Journal of Geophysical Research, Oceans 121, 4833–4853.
Goodwin, I.D., Ribo, M., Mortlock, T., 2020. Coastal sediment compartments, wave climate and centennial-scale sediment budget: the south-eastern Australian example. In: Jackson, D., Short, A. (Eds.), Sandy Beach Morphodynamics. Elsevier, pp. 615–640 (Chapter 25).
Hein, C., Ashton, A., 2020. Long-term shoreline morphodynamics: processes and preservation of environmental signals. In: Jackson, D.W.T., Short, A.D. (Eds.), Sandy Beach Morphodynamics. https://doi.org/10.1016/B978-0-08-102927-5.00021-7.
Hemer, M.A., Church, J.A., Hunter, J.R., 2010. Variability and trends in the directional wave climate of the Southern Hemisphere. Int. J. Climatol. 30, 475–491.
Hibbert, F.D., et al., 2016. Coral indicators of past sea-level change: a global repository of U-series dated benchmarks. Quat. Sci. Rev. 145, 1–56.
Hill, K.L., Rintoul, S.R., Ridgway, K.R., Oke, P.R., 2011. Decadal changes in the South Pacific western boundary current system revealed in observations and ocean state estimates. J. Geophys. Res. 116, C01009. https://doi.org/10.1029/2009JC005926.
Hoggard, M.J., Czarnota, K., Richards, F.D., Huston, D.L., Jaques, A.L., Ghelichkhan, S., 2020. Global distribution of sediment-hosted metals controlled by craton edge stability. Nat. Geosci. 13, 504–510.
Hsu, J.R.C., Evans, C., 1989. Parabolic bay shapes and applications. Proceedings of the Institute of Civil Engineers 87 (2), 557–570. Thomas Telford, London.
Hsu, J.R.C., Yu, F.-C., Benedet, L., 2010. Static bay beach concept for scientists and engineers: a review. Coast. Eng. 57, 76–91, 2010.
James, N.P., Martindale, R.C., Malcolm, I., Bone, Y., Marshall, J., 2004. Surficial sediments on the continental shelf of Tasmania, Australia. Sediment. Geol. 211, 33–52, 2008.
Jenkin, J.J., 1968. The geomorphology and upper cainozoic geology of south-east Gippsland, Victoria. Geol. Surv. Vic. Mem. vol. 27, 152.
Jennings, J.N., 1959. The coastal geomorphology of king island, Bass Strait. In: Relation to Changes in the Relative Level of Land and Sea. Rec. Q. Vict. Mus.> N.S. Ll, p. 39.
Jennings, J.N., 1961. Sealevel Changes in King Island, Bass Strait. *Zeitschriftfür Geomorphologie* NF3, pp. 80–84.
Jutson, J.T., 1927. Notes on the coastal physiography of Port Campbell Victoria. Proc. Roy. Soc. Vic. 40, 45–57.
Kendall, R., Mitrovica, J.X., Milne, G.A., 2005. On post glacial sea-level: II. Numerical formulation and comparative results on spherically-symmetric Earth models. Geophys. J. Int. 161, 679–706.
Klein, A.H.F., Vargas, A., Raabe, A.L.A., Hsu, J.R.C., 2003. Visual assessment of bayed beach stability using computer software. Comput. Geosci. 29, 1249–1257.
Kopp, R.E., Simons, F.J., Mitrovica, J.X., Maloof, A.C., Oppenheimer, M., 2009. Probabilistic assessment of sea level during the last interglacial. Nature 462, 863–867.
Kopp, R.E., Simons, F.J., Mitrovica, J.X., Maloof, A.C., Oppenheimer, M., 2013. A probabilistic assessment of sea level variations within the last interglacial stage. Geophys. J. Int. 193, 711–716.
Lambeck, K., Purcell, A., Funder, S., Kjaer, K.H., Larsen, E., Moller, P., 2006. Constraints on the Late Saalian to early Middle Weichselian ice sheet of Eurasia from field data and rebound modeling. Boreas 35, 539–575.
Lambeck, K., Purcell, A., Dutton, A., 2012. The anatomy of interglacial sea levels: the relationship between sea levels and ice volumes during the Last Interglacial. Earth Planet Sci. Lett. 315–316, 4–11.
Lamy, F., et al., 2019. Precession modulation of the South Pacific westerly wind belt over the past million years. Proc. Natl. Acad. Sci. USA 116 (47), 23455–23460. www.pnas.org/cgi/doi/10.1073/pnas.1905847116.
Liu, J., Meucci, A., Liu, Q., Babanin, A.V., Ierodiaconou, D., Young, I.R., 2022. The wave climate of Bass Strait and south-east Australia. Ocean Model. https://doi.org/10.1016/j.ocemod.2022.101980.
Lorscheid, T., Rovere, A., 2019. The indicative meaning calculator – quantification of paleo sea-level relationships by using global wave and tide datasets. Open Geospatial Data, Software and Standards 4, 10. https://doi.org/10.1186/s40965-019-0069-8, 2019.
Lucas, C., Timbal, B., Nguyen, H., 2014. The expanding tropics: a critical assessment of the observational and modeling studies. WIREs Clim. Change 5, 89–112. https://doi.org/10.1002/wcc.251.
Malikides, M., Harris, P.T., Jenkins, C.J., Keene, J.B., 1988. Carbonate sandwaves in Bass Strait. Aust. J. Earth Sci. 35, 303–311.
Marshall, G.J., 2003. Trends in the southern annular mode from observations and reanalyses. J. Clim. 16, 4134–4143. https://doi.org/10.1175/1520-0442(2003)016< 4134:titsam> 2.0.co.
Marshall, J.F., Thom, B.G., 1976. The sea level in the last interglacial. Nature 263, 120–121.
Masselink, G., Kroon, A., Davidson-Arnott, R.G.D., 2006. Morphodynamics of intertidal bars in wave-dominated coastal settings – a review. Geomorphology 73, 33–49.
McCulloch, M.T., Esat, T., 2000. The coral record of Last Interglacial sea levels and sea surface temperatures. Chem. Geol. 169, 107–129.
McCulloch, M.T., Mortimer, G.E., 2008. Applications of the ^{238}U-^{230}Th decay series to dating of fossil and modern corals using MC-ICPMS. Aust. J. Earth Sci. 55 (6), 955–965. https://doi.org/10.1080/08120090802097435.
McInnes, K.L., Hubbert, G.D., 2003. A numerical modelling study of storm surges in Bass Strait. Aust Met Mag 52, 143–156.
McInnes, K.L., O'Grady, J.G., Hubbert, G.D., 2009. Modelling sea level extremes from storm surges and wave setup for climate change assessments in Southeastern Australia. J Coast Res, SI 56. Proceedings of the 10th International Coastal Symposium), 1005 – 1009, Lisbon, Portugal.
McSweeney, S., 2020. Temporal and spatial variability of the open coast wave climate of Victoria, Australia. Mar. Freshw. Res. 71, 394–413. https://doi.org/10.1071/MF18489.
Mitrovica, J.X., Milne, G.A., 2002. On the origin of Late Holocene highstands within equatorial ocean basins. Quat. Sci. Rev. 21, 2179–2190.
Mitrovica, J.X., Wahr, J., Matsuyama, I., Paulson, A., 2005. The rotational stability of an ice-age Earth. Geophys. J. Int. 161, 491–506.
Mortlock, T.R., Goodwin, I.D., 2015. Directional wave climate and power variability in the Tasman Sea. Continent. Shelf Res. 98, 36–53.
Mortlock, T.R., Goodwin, I.D., 2018a. Robbins Island Metocean and Coastal Processes Study: Phase 1 Report, 2018. A report prepared by Macquarie University and Risk Frontiers, for the GHD Australia, p. 63 (available from: the authors).
Mortlock, T.R., Goodwin, I.D., 2018b. Robbins Island Metocean and Coastal Processes Study: Phase 2 Report. A Report Prepared by Macquarie University and Risk Frontiers, for the GHD Australia. November 2018 (available from: the authors).
Mount, R., Prahalad, V., Sharples, C., Tilden, J., Morrison, B., Lacey, M., Ellison, J., Helman, M., Newton, J., 2010. Circular Head Region Foreshore Habitats: Sea

Level Risk Vulnerability Assessment: Final Report. A Technical Report to Cradle Coast NRM Region and the Cradle Coast Authority Prepared by the Blue Wren Group, vol. 221. School of Geography and Environmental Studies, University of Tasmania. July 2010.
Murray, A.S., Wintle, A.G., 2000. Luminescence dating of quartz using an improved single-aliquot regenerative-dose protocol. Radiat. Meas. 32, 57–73.
Murray-Wallace, C.V., Beu, A.G., Kendrick, G.W., Brown, L.J., Belperio, A.P., Sherwood, J.E., 2000. Palaeoclimatic implications of the occurrence of the arcoid bivalve Anadara trapezia (Deshayes) in the Quaternary of Australasia. Quat. Sci. Rev. 19, 559–590.
Murray-Wallace, C.V., Belperio, A.P., Dosseto, A., Nicholas, W.A., Mitchell, C., Bourman, R.P., Eggins, S.M., Grun, R., 2016. Last interglacial (MIS 5e) sea-level determined from a tectonically stable, far-field location, Eyre Peninsula, southern Australia. Aust. J. Earth Sci. 63, 611–630.
Oliver, T.S., Kennedy, D.M., Tamura, T., Murray-Wallace, C.V., Konlechner, T.M., Augustinus, P.C., Woodroffe, C.D., 2018. Interglacial-glacial climatic signatures preserved in a regressive coastal barrier, southeastern Australia. Palaeogeogr. Palaeoclimatol. Palaeoecol. 501, 124–135.
Murray-Wallace, C.V., Goede, A., 1995. Aminostratigraphy and electron spin resonance dating of Quaternary coastal neotectonism in Tasmania and the Bass Strait islands. Aust. J. Earth Sci. 42 (1), 51–67.
O'Grady, J.G., McInnes, K.L., 2010. Wind waves and their relationship to storm surges in northeastern Bass Strait. Aust Met Ocean J 60, 265–275.
O'Leary, M.J., et al., 2013. Ice sheet collapse following a prolonged period of stable sea level during the last interglacial. Nat. Geosci. 6, 706–800.
Pan, T.Y., Murray-Wallace, C.V., Dosseto, A., Bourman, R.P., 2020. The last interglacial (MIS 5e) sea level highstand from a tectonically stable far-field setting, Yorke Peninsula, southern Australia. Mar. Geol. 398, 126–136. https://doi.org/10.1016/j.margeo.2018.01.012.
Pariwono, J.I., Bye, J.A.T., Lennon, G.W., 1986. Long-period variations of sea-level in Australasia. Geophys. J. Roy. Astron. Soc. 87 (1), 43–54.
Pickett, J.W., 1981. A late Pleistocene coral fauna from Evans Head. N.S.W. Alcheringa 5, 71–83.
Pickett, J.W., Ku, T.L., Thompson, C.H., Roman, D., Kelley, R.A., Huang, Y.P., 1989. Review of age determinations on Pleistocene corals in eastern Australia. Quat. Res. 31, 392–395.
Porter-Smith, R., Harris, P.T., Andersen, O.B., Coleman, R., Greenslade, D., Jenkins, C.J., 2004. Classification of the Australian continental shelf based on predicted sediment threshold exceedance from tidal currents and swell. Mar. Geol. 211, 1–20, 2004.
Reeckman, S.A., Gill, E.D., 1981. Rates of vadose diagenesis in Quaternary dune and shallow marine calcarenites, Warrnambool, Victoria, Australia. Sediment. Geol. 30, 157–172.
Reid, J.S., Fandry, C.B., 1994. Wave Climate Measurements in the Southern Ocean. CSIRO Marine Laboratories – Report, vol. 223. CSIRO Australia, p. 117.
Richards, F.D., Hoggard, M.J., White, N., Ghelichkhan, S., 2002. Exploring the relationship between upper mantle structure and short wavelength dynamic topography using calibrated anelasticity parameterizations. J. Geophys. Res. Solid Earth 125, e2019JB019062.
Ridgway, K.R., 2007. Seasonal circulation around Tasmania: an interface between eastern and western boundary dynamics. J. Geophys. Res. 112, C10016. https://doi.org/10.1029/2006JC003898.
Rohling, E.J., et al., 2019. Asynchronous Antarctic and Greenland ice-volume contributions to the last interglacial sea-level highstand. Nat. Commun. 10, s41467.
Rovere, A., Raymo, M.E., Vacchi, M., Lorscheid, T., Stocchi, P., Gómez-Pujol, L., Harris, D.L., Casella, E., O'Leary, M.J., Hearty, P.J., 2016. The analysis of last interglacial (MIS 5e) relative sea-level indicators: reconstructing Sea-level in a warmer world. Earth Sci. Rev. 159, 404–427. https://doi.org/10.1016/j.earscirev.2016.06.006.
Roy, P.S., Cowell, P.J., Ferland, M.A., Thom, B.G., 1994. Wave dominated coasts. In: Carter, R.W.G., Woodroffe, C.D. (Eds.), Coastal Evolution—Late Quaternary Shoreline Morphodynamics. Cambridge University Press, Cambridge, U.K., pp. 121–186
Scott, T., Masselink, G., Russell, P., 2011. Morphodynamic characteristics and classification of beaches in England and Wales. Mar. Geol. 286, 1–20.
Shennan, I., 2015. Handbook of sea-level research. In: Handbook of Sea-Level Research. Wiley, Chichester, pp. 3–25. https://doi.org/10.1002/9781118452547.ch2.
Short, A.D. (Ed.), 1999. Beach and Shoreface Morphodynamics. John Wiley and Sons, Chichester, p. 379.
Short, A.D., 2006a. Australian beach systems — nature and distribution. J. Coast Res. 22, 11–27.
Short, A.D., 2006b. Beaches of the Tasmanian Coast and Islands: a Guide to Their Nature, Characteristics, Surf and Safety. Sydney University Press, University of Sydney, p. 362. March 2006.
Short, A.D., 2020. Wave-dominated, tide-modified and tide-dominated continuum. In: Jackson, D., Short, A. (Eds.), Sandy Beach Morphodynamics. Elsevier, pp. 363–389 (Chapter 16).
Simons, F.J., van der Hilst, R.D., 2002. Age-dependent seismic thickness and mechanical strength of the Australian lithosphere. Geophys. Res. Lett. 29. https://doi.org/10.1029/2002gl014962, 2002.
Stockdon, H.F., Holman, R.A., Howd, P.A., Sallenger, A.H., 2006. Empirical parameterization of setup, swash, and runup. Coast. Eng. 53, 573–588.
Storms, J.E.A., Weltje, G.J., van Dijke, J.J., Geel, C.R., Kroonenberg, S.B., 2002. Process-response modeling of wave- dominated coastal systems: simulating evolution and stratigraphy on geological timescales. J. Sediment. Res. 72, 226–239.
Sturman, A., Tapper, N., 2006. The Weather and Climate of Australia and New Zealand, second ed. Oxford University Press, p. 541pp.
Sutherland, F.L., Kershaw, R.C., 1971. The cainozoic geology of Flinders island, Bass Strait. Pap. Proc. R. Soc. Tasman. 105, 151–175.
Tamura, T., 2012. Beach ridges and prograded beach deposits as palaeoenvironment records. Earth Sci. Rev. 114, 279–297, 2012.
Tamura, T., Nicholas, W.A., Oliver, T.S.N., Brooke, B.P., 2018. Coarse-sand beach ridges at Cowley Beach, North-Eastern Australia: their formative processes and potential as records of tropical cyclone history. Sedimentology 65, 721–744.
Timbal, B., Drosdowsky, W., 2012. The relationship between the decline of Southern Australian rainfall and the strengthening of the subtropical ridge. Int. J. Climatol. 33 (4), 1021–1034. https://doi.org/10.1002/joc.3492.
Van de Geer, G., 1981. Late Quaternary Marine and Freshwater Swamp Deposits of Northwestern Tasmania. Unpublished Ph.D thesis, Department of Geography, University of Tasmania.
Van de Geer, G., Colhoun, E.A., Bowden, A., 1979. Evidence and problems of Interglacial marine deposits in Tasmania. Geol. Mijnbouw 58, 29–32.
Van de Plassche, O., 1986. Introduction. In: van de Plassche, O. (Ed.), Sea-level Research: a Manual for the Collection and Evaluation of Data. Springer Netherlands, Dordrecht, pp. 1–26. https://doi.org/10.1007/978-94-009-4215-8_1.
Waelbroeck, C., Labeyrie, L., Michel, E., Duplessy, J.C., 2002. Sea-level and deep water temperature changes derived from benthic foraminifera isotopic records. Quat. Sci. Rev. 21, 295–305.
White, N.J., et al., 2014. Australian sea levels—trends, regional variability and influencing factors. Earth Sci. Rev. 136, 155–174, 2014.
Wijeratne, E.M.S., Pattiaratchi, C.B., Eliot, M., Haigh, I.D., 2012. Tidal characteristics in Bass Strait, south-east Australia. Estuar. Coast Shelf Sci. 114, 156–165, 2012.